2-D numerical study of hydrated wedge dynamics from subduction to post-collisional phases

Alessandro Regorda, Manuel Roda, Anna Maria Marotta and M. Iole Spalla

Dipartimento di Scienze della Terra 'A. Desio', Università degli Studi di Milano, via Mangiagalli 34, I-20133 Milano, Italy.
E-mail: alessandro.regorda@unimi.it

SUMMARY

We developed a 2-D finite element model to investigate the effect of shear heating and mantle hydration on the dynamics of the mantle wedge area. The model considers an initial phase of active oceanic subduction, which is followed by a post-collisional phase characterized by pure gravitational evolution. To investigate the impact of the subduction velocity on the thermomechanics of the system, three models with different velocities prescribed during the initial subduction phase were implemented. Shear heating and mantle hydration were then systematically added into the models. We then analysed the evolution of the hydrated area during both the subduction and post-collisional phases, and examined the difference in P_{max}–T (maximum pressure–temperature) and P–T_{max} (pressure–maximum temperature) conditions for the models with mantle hydration. The dynamics that allow for the recycling and exhumation of subducted material in the wedge area are strictly correlated with the thermal state at the external boundaries of the mantle wedge, and the size of the hydrated area depends on the subduction velocity when mantle hydration and shear heating are considered simultaneously. During the post-collisional phase, the hydrated portion of the mantle wedge increases in models with high subduction velocities. The predicted P–T configuration indicates that contrasting P–T conditions, such as Barrovian- to Franciscan-type metamorphic gradients, can contemporaneously characterize different portions of the subduction system during both the active oceanic subduction and post-collisional phases and are not indicative of collisional or subduction phases.

Key words: Numerical modelling; Continental margins: convergent; Heat generation and transport; Subduction zone processes.

1 INTRODUCTION

The exhumation mechanisms of both subducted oceanic and continental lithospheres have been widely explored to unravel the dynamics of orogenic belt accretion (e.g. Dal Piaz 1972; Cloos 1982; Platt 1986, 1993; Shreve & Cloos 1986; Cloos & Shreve 1988; Polino *et al.* 1990; Tao & O'Connell 1992; Spalla *et al.* 1996; Duchene *et al.* 1997; Guillot *et al.* 2009; Maierovà *et al.* 2016). Numerical and petrological models have demonstrated the dominant role of mantle wedge hydration in the cyclic uplift and burial of deeply subducted material prior to continental collision (e.g. Gerya *et al.* 2002; Gorczyk *et al.* 2006, 2007; Yamato *et al.* 2007; Ernst & Liou 2008; Agard *et al.* 2009; Meda *et al.* 2010; Roda *et al.* 2010, 2012; Le Voci *et al.* 2014). In ocean–continent subduction systems, low viscosity hydrated mantle facilitates the exhumation and underplating of subducted oceanic and continental material at the base of the crust of the upper plate (Billen & Gurnis 2001; Hirth & Kohlstedt 2003; Billen 2008; Hirth & Guillot 2013;

Nagaya *et al.* 2016). When hydration is not considered, a dry and stiff mantle buttress characterizes the wedge area and strongly affects the thermomechanical regime during the subduction stage and subsequent continental collision (Marotta & Spalla 2007; Spalla & Marotta 2007; Gerya *et al.* 2008; Meda *et al.* 2010). In this scenario, both crustal thickening and heat supplied from radiogenic decay are mainly driven by the burial of the continental crust of the lower plate during collision (e.g. Marotta & Spalla 2007; Spalla & Marotta 2007). Additional heat can be supplied by shear heating, affecting the thermal state of subduction zones and, thus, the rheology of the system (e.g. Gerya & Yuen 2003; Burg & Gerya 2005; Gerya & Stoeckhert 2006; Gerya *et al.* 2008; Hartz & Podladchikov 2008; Thielmann & Kaus 2012; Minakov *et al.* 2013; Souche *et al.* 2013).

To investigate the effects of shear heating and mantle wedge hydration on the thermal state and dynamics of an ocean/continent subduction system, we developed a 2-D thermomechanical model in which an initial phase of active oceanic subduction with different

prescribed velocities is followed by a post-collisional phase, characterized by the absence of prescribed velocities and driven by gravitational forces only. Results of the models with shear heating and/or mantle hydration are compared to models with no shear heating and no hydration (Marotta & Spalla 2007), and we then analyse the effects of these parameters on both the strain rate and the viscosity. The effects of the subduction velocities on the size and evolution of the hydrated area are also analysed. Finally, predictions of the pressure–temperature (*P–T*) conditions of crustal markers and the thermal field characterizing different portions of subduction systems are used to discuss the metamorphic environments in different portions of subduction/collision setting.

2 MODEL FORMULATION

The model simulates the thermomechanical evolution of a crust-mantle system during two tectonic phases: (1) an active oceanic subduction phase during convergence of a continent–ocean–continent system that drives the closure of a 2500-km-wide ocean and (2) a post-collisional phase after continental collision.

The physics of the crust–mantle system during the two tectonic phases are described by the equations for the conservation of mass, momentum and energy, which include the extended Boussinesq approximation (e.g. Christensen & Yuen 1985) for incompressible fluids. These equations are expressed as follows:

$$\nabla \cdot \vec{u} = 0, \tag{1}$$

$$-\nabla P + \nabla \cdot \vec{\tau} + \rho \vec{g} = 0, \tag{2}$$

$$\rho c_p \left(\frac{\partial T}{\partial t} + \vec{u} \cdot \nabla T \right) = \nabla \cdot (K \nabla T) + H_r + H_s + H_a, \tag{3}$$

where $\vec{u}$ represents the velocity, P represents the pressure, $\vec{\tau}$ represents the deviatoric stress, ρ represents the density, $\vec{g}$ represents gravitational acceleration, c_p represents the specific heat at a constant pressure, T represents the temperature, K represents the thermal conductivity, H_r represents the radiogenic heating, $H_s = \tau_{ij} \dot{\epsilon}_{ij}$ represents the shear heating, $H_a = T\alpha \frac{DP}{Dt} \approx -\alpha T \rho \vec{g} v_y$ represents the adiabatic heating and α represents the thermal coefficient of expansion. In the following we refer to total energy as $H_{tot} = H_r + H_s + H_a$. Because the mantle has a very high Prandtl number, we neglected inertial terms when writing Equation 2. Equations 1, 2 and 3 are numerically integrated via the 2-D finite element (FE) thermomechanical code SubMar (Marotta *et al.* 2006), which uses the penalty function formulation to integrate the conservation of momentum equation and the Petrov–Galerkin method to integrate the conservation of energy equation.

The original code has been modified to include new constraints on the composition, energy and mantle-hydration mechanism. The model combines a viscous rheology for the sublithospheric mantle with a brittle/plastic rheology for the lithosphere. Water trapped within the subducting oceanic plate is transported to large depths (e.g. Liu *et al.* 2007; Faccenda 2014; Rosas *et al.* 2016). The oceanic plate is then dehydrated because of the increased temperature and pressure (Schmidt & Poli 1998; Liu *et al.* 2007; Faccenda *et al.* 2009; Faccenda & Mancktelow 2010). The water released by the slab hydrates the mantle wedge and can lead to its serpentinization and to a decrease in viscosity (Gerya *et al.* 2002; Honda & Saito 2003; Arcay *et al.* 2005). We simulate the rheological weakening of the mantle wedge by assuming a constant viscosity of 10^{19} Pa s and a density of

3000 kg m^{-3} for the mantle occurring at the pressure and temperature conditions described by the stability field of serpentine (Honda & Saito 2003; Arcay *et al.* 2005; Gerya & Stoeckert 2006; Roda *et al.* 2010). We neglect the effects of water migration because of the expected very high water velocities compared with the chosen time steps and total computational time (Quinquis & Buiter 2014); thus, hydration can be considered instantaneous in our model. The latent heat of serpentinization is also neglected because it is balanced by the latent heat produced by de-serpentinization and melting at large scales (Pérez-Gussinyé & Reston 2001; Rupke *et al.*, 2004, 2013). Furthermore, it has been suggested that a latent heat of serpentinization of 2.9×10^5 J kg^{-1} (Emmanuel & Berkowitz 2006) results in an increase in temperature of 300 °C (Rupke *et al.* 2013); therefore, the serpentine would cease to be stable. However, since serpentinization occurs on a large scale, the latent heat of hydration-dehydration must have a minor impact on the thermal field because the circulation of fluids is an efficient mechanism of transferring heat. In addition, because another aim of this study is to verify how shear heating could impact the thermodynamics of the system, considering other sources of heat would increase the difficulty of identifying the effects of the different mechanisms. Further details on the implementation of the rheology and the mantle hydration mechanism are in Appendix A.

The numerical integration is performed in a 2-D rectangular domain that is 1400 km wide and 700 km deep (Fig. 1). The domain is discretized by a non-deforming irregular grid composed of 4438 quadratic triangular elements and 9037 nodes, and it has a denser nodal distribution near the contact region between the plates, where the most significant gradients in temperature and velocity fields are expected. The size of the elements varies horizontally from 10 to 80 km and vertically from 5 to 20 km, and smaller elements are located in the active margin region up to depths of 300 km.

To differentiate the crust from the mantle, we use the Lagrangian particle technique (e.g. Christensen 1992), which is implemented as specified in Appendix A. Table 1 summarizes the material properties and rheological parameters.

The boundary conditions are set in terms of the velocities and temperatures prescribed at the boundaries of the 2-D domain. The velocity boundary conditions correspond to stress-free conditions assumed along the upper boundary of the 2-D domain, and no-slip conditions assumed along the other boundaries (Fig. 1). In addition, during the active oceanic subduction phase, a velocity of 3, 5 or 8 cm yr^{-1} is prescribed along the bottom of the oceanic crust, that drives the closure of the 2500-km-wide ocean in 85.5, 51.5 and 32 Ma, respectively. Velocities of 3 and 8 cm yr^{-1} have been chosen to describe slower and faster subduction zones (observed respectively in portions of Central and in South America and the Philippines, Cruciani *et al.* 2005; Lallemand *et al.* 2005), respectively. The velocity of 5 cm yr^{-1} has been chosen to represent a moderate velocity convergence system, which is consistent with the model described by Marotta & Spalla (2007). To facilitate the subduction of the oceanic lithosphere, the same velocity is also fixed along a 45° dipping plane that extends from the trench to a depth of 100 km. Differently, during the post-collisional phase, the system undergoes a pure gravitational evolution.

The thermal boundary conditions correspond to fixed temperatures at the top (300 K) and the bottom (1600 K) of the model, zero thermal flux at the right vertical sidewall 'a' and fixed temperature along the left side. The initial thermal structure corresponds to a simple conductive thermal configuration throughout the lithosphere, with temperatures that vary from 300 K at the surface to
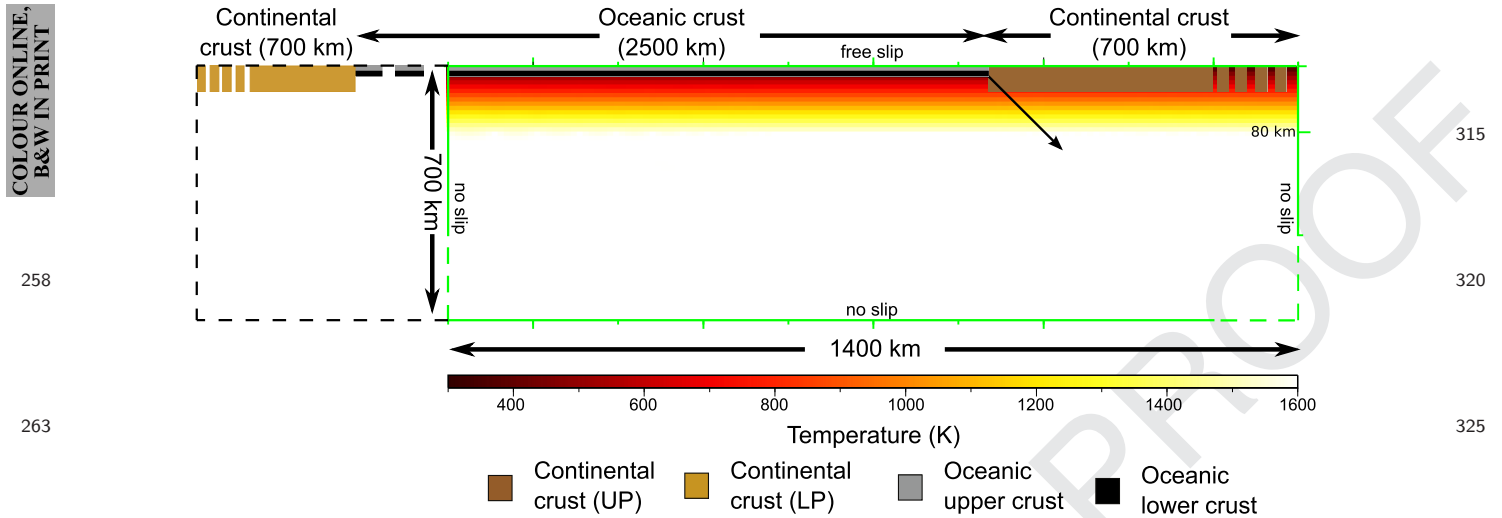
Figure 1. Setup, boundary conditions and initial thermal configuration of the numerical model. The distances are not to scale. Green lines circumscribe the area where numerical solution is performed. UP stands for upper plate; LP stands for lower plate.

Table 1. Values of the material and rheological parameters used in the analysis.

	Continental crust	Upper oceanic crust	Lower oceanic Crust	Mantle	Serpentine
Rheology	Dry Granite	–	Diabase	Dry Dunite	–
E (kJ mol^{-1})	123	–	260	444	–
n	3.2	–	2.4	3.41	–
μ_0(Pa s)	3.47×10^{21}	10^{19}	1.61×10^{22}	5.01×10^{20}	10^{19}
ρ_0(kg m^{-3})	2640	2961	2961	3200	3000
K(W m^{-1} K^{-1})	3.03	2.10	2.10	4.15	4.15
H_c(μWm^{-3})	2.5	0.4	0.4	0.002	0.002
References	[a, d, f]	[b, f, i, j, k]	[a, b, c, f]	[c, d, e, f, j]	[d, f, g, h, i]

[a]Ranalli & Murphy (1987); [b]Afonso & Ranalli (2004); [c]Kirby (1983); [d]Haenel *et al.* (1988); [e]Chopra & Peterson (1981); [f]Dubois & Diament (1997), Best & Christiansen (2001); [g]Roda *et al.* (2011); [h]Schmidt & Poli (1998); [i]Gerya & Stockhert (2006); [j]Roda *et al.* (2012); [k]Gerya & Yuen (2003).

1600 K at its base, and a constant temperature of 1600 K below the lithosphere. The base of the lithosphere is located at a depth of 80 km under both the oceanic and continental domains. This configuration corresponds to both an oceanic lithosphere of approximately 40 Ma, based on the cooling of a semi-infinite half space model (Turcotte & Schubert 2002) and a thinned continental passive margin based on a medium to slow spreading rate of 2–3 cm yr^{-1} (e.g. Marotta *et al.* 2016). The 1600 K isotherm defines the base of the lithosphere throughout the evolution of the system.

Four model sets have been developed to analyse the impact of shear heating and mantle hydration on the thermomechanics of the system. We list the acronyms and setup of the models in Table 2. REF indicates the reference models without shear heating or mantle hydration (Appendix B), SH represents models with shear heating and without mantle hydration, MH represents models without shear heating and with mantle hydration, and SH+MH represents models with both shear heating and mantle hydration.

3 MODEL RESULTS

The model results are illustrated as follows: we first describe differences in the global thermomechanics (Section 3.1) as a function of the prescribed velocities, the occurrence of shear heating (SH models), mantle hydration (MH models) or both mechanisms at the same time (SH+MH models) with respect to REF models (Appendix B). Then we analyse the evolution of the hydrated area (Section 3.2) for the MH models and SH+MH models. Finally, we present the

differences in the P_{max}–T and P–T_{max} conditions for simulations with mantle hydration (Section 3.3) without (MH models) or with (SH+MH models) shear heating. Main results are also synthesized in Tables 3 and 4.

3.1 Global thermomechanics

Since the reference model (REF) has been already extensively described in a previous papers (Marotta & Spalla 2007), the upgrades of the REF model and its thermomechanical evolution are synthesized in Appendix B.

3.1.1 Effect of shear heating (SH models)

The introduction of shear heating does not significantly impact the large-scale thermomechanics of the system throughout the active oceanic subduction phase. Rather, a significant increase in temperature is observed on a smaller scale in the mantle wedge and the subducting oceanic lithosphere (see the isotherms in Fig. 2a). In fact, the 1500 K isotherm in the mantle wedge rises, in the different models, from approximately 80 km in the REF.3 to 60 km in the SH.3, from 60 km in the REF.5 to 20 km in the SH.5 and from 50 km in the REF.8 to 15 km in the SH.8. Moreover, within the subducting lithosphere, the maximum depth reached by the 800 K isotherm remains shallower for all SH models (Fig. 2a) compared with the REF models, which suggests a warmer thermal state. The increase of temperature in the subducting oceanic lithosphere results

Table 2. Characteristics and acronyms of the models.

	REF (Appendix B)	SH	MH	SH+MH
Velocity (cm yr^{-1})	No shear heating No mantle hydration	Shear heating	Mantle hydration	Shear heating Mantle hydration
3	REF.3	SH.3	MH.3	SH+MH.3
5	REF.5 (Marotta & Spalla 2007)	SH.5	MH.5	SH+MH.5
8	REF.8	SH.8	MH.8	SH+MH.8

Table 3. Synthesis of the results for the thermomechanical evolution of the models.

		REF (Appendix B)	SH	MH	SH+MH
Thermomechanics of the system	Active oceanic subduction phase	Activation of large-scale mantle flow	Activation of large-scale mantle flow	Activation of large-scale mantle flow	Decreasing in the intensity of large-scale mantle flow
		Thermomechanical erosion of the upper plate	Thermomechanical erosion of the upper plate	Less erosion of the upper plate with respect to REF model	Less erosion of the upper plate with respect to REF model
		Increase of T in the wedge with the increase of subduction velocity	Increase of T in the wedge with the increase of subduction velocity	Increase of T in the wedge with the increase of subduction velocity	T in the wedge does not depend on the subduction velocity
		Decrease of T in the slab with the increase of subduction velocity	Decrease of T in the slab with the increase of subduction velocity	Decrease of T in the slab with the increase of subduction velocity	Decrease of T in the slab with the increase of subduction velocity
			Increase of T in the mantle wedge and subducting plate with respect to REF		Increase of T in the mantle wedge and subducting plate with respect to REF
				Activation of short-wavelength convective cells in the wedge	Activation of short-wavelength convective cells in the wedge
				Recycling of subducted material	Recycling of subducted material
					Decrease of extension of the hydrated area with respect to MH
		Total energy of the system function of the radiogenic heat	Total energy of the system function of the radiogenic heat and shear heating	Total energy of the system function of the radiogenic heat	Total energy of the system function of the radiogenic heat and shear heating
	Post-collisional phase	Decrease of the intensity of mantle flow of 1 order of magnitude	Decrease of the intensity of mantle flow of 1 order of magnitude	Decrease of the intensity of mantle flow of 1 order of magnitude	Decrease of the intensity of mantle flow of 1 order of magnitude
		Rising of the subducted slab	Rising of the subducted slab	Rising of the subducted slab and doubling of the crust	Rising of the subducted slab and doubling of the crust
		Thermal re-equilibration of the system	Thermal re-equilibration of the system	Thermal re-equilibration of the system and additional heat by radiogenic decay	Thermal re-equilibration of the system and additional heat by radiogenic decay
			Negligible effect of shear heating		Negligible effect of shear heating
				Dehydration of the wedge	Dehydration of the wedge

in a lower slab dip, because of the lower density contrast between lithospheric and asthenospheric mantle.

The higher temperatures predicted in the wedge area are caused by the large amount of energy produced by shear heating, which is here up to six orders of magnitude higher than in the upper plate (Fig. 2a$_3$), where energy is primarily generated by radiogenic heat.

Thus, the total energy in the wedge area is approximately one order of magnitude higher than that in the continental crust and up to five orders of magnitude higher than that predicted by the REF model (Fig. 2a$_4$). An increase in the prescribed subduction velocity corresponds to a slight increase in energy produced by shear heating (less than one order of magnitude) because the increased strain rate

Table 4. Synthesis of the results for the evolution of the hydrated area and for *P–T* recorded by models with mantle hydration.

		MH	SH+MH
Evolution of the hydrated area	Active oceanic subduction phase	Velocity of hydration increase with the increase of subduction velocity	Velocity of hydration increase with the increase of subduction velocity
		The extension of the main hydrated area decrease with the increase of subduction velocity	The extension of the main hydrated area increase with the increase of subduction velocity
		During early stages, the lower the subduction velocity, the smaller the hydrated area	During the entire evolution the lower the subduction velocity, the smaller the hydrated area
		During advanced stages, the lower the velocity the larger the hydrated area	
			Decrease of extension of the hydrated area with respect to MH
	Post-collisional phase	Initial extension of the hydrated area toward the external portion of the wedge	Initial extension of the hydrated area toward the external portion of the wedge
		Successive rapid decrease of extension of the hydrated area	Successive rapid decrease of extension of the hydrated area
			Lesser duration of the hydrated area with respect to MH
P–T	Active oceanic subduction phase	Coexistence of *P–T* conditions characterized by intermediate and high *P/T* ratios	Coexistence of *P–T* conditions characterized by intermediate and high *P/T* ratios
		The thermal state does not change in time	The thermal state does not change in time
		Oceanic and subducted continental markers never record Barrovian metamorphism during exhumation	Subducted markers never record Barrovian metamorphism during exhumation
			Maximum temperatures are higher with respect to MH
	Post-collisional phase	Migration of *P–T* conditions recorded toward higher *T*	Migration of *P–T* conditions recorded toward higher *T*
		Maximum temperatures are recorded at the end of the evolution	Maximum temperatures are recorded at the end of the evolution
		Subducted markers record Barrovian metamorphism during exhumation	

is counterbalanced by a decrease in the viscosity due to the local increase in temperature.

During the post-collisional phase, the thermal state is comparable to that predicted by the REF models because the strain rate (Fig. 2b$_2$) is very low and the energy produced by shear heating (Fig. 2b$_3$) is negligible with respect to the radiogenic energy. Therefore, the total energy predicted by the SH models (Figs 2b$_4$) is comparable to that predicted by the REF models.

3.1.2 *Effect of mantle hydration (MH models)*

During the active oceanic subduction phase, the introduction of mantle hydration causes a decrease of friction between the two plates, which leads to a smaller amount of eroded crustal material from the upper plate (Fig. 3a) with respect to REF model. However, mantle hydration greatly affects the dynamics in the mantle wedge area, and short-wavelength convective cells appear in the low-viscosity hydrated domain that favour the recycling of continental crust eroded from the upper plate together with the upper oceanic crust that derives from the subducting lithosphere (Fig. 3a). The recycling and mixing of large amounts of continental and oceanic crust and mantle slices are consistent with other models that consider mantle hydration (e.g. Gerya & Yuen 2003; Stockhert & Gerya 2005; Roda *et al.* 2012; Li *et al.* 2015) and has a cooling effect inside the wedge preventing the large-scale convective

flows from reaching the internal portion of the wedge (see isotherm 1500 K in Fig. 3a). The small-scale convective cells remain active throughout the active oceanic subduction phase (Fig. 3a).

Because the MH models do not account for the shear heating, the total energy depends exclusively on radiogenic heat, which is up to three orders of magnitude higher in the continental crust than in the mantle (Fig. 4a$_3$). The large amount of recycled continental crustal material is responsible for the increase in the radiogenic energy in the hydrated mantle wedge, which is approximately one to two orders of magnitude higher than that in the dry mantle and one to two orders of magnitude less than that in the continental crust (Fig. 4a$_3$). However, the increase in the radiogenic energy in the hydrated wedge does not balance the cooling induced by the lack of large-scale convective flows in this area, and the temperature in the mantle wedge remains lower than that in the REF models.

During the active oceanic subduction phase, the viscosity inside the cold subducting lithospheric mantle (red in Fig. 4a$_1$) is approximately two to three orders of magnitude higher than the viscosity in the dry area of the mantle wedge (light blue in Fig. 4a$_1$) and up to six orders of magnitude higher than the viscosity in the hydrated domain (blue in Fig. 4a$_1$). In addition, the strain rate is very high in both the lower plate and the wedge area and varies from 10^{-16} s^{-1} in the lower plate to 10^{-13} s^{-1} near the subduction zone and in the wedge area (Fig. 4a$_2$). The maximum strain rate is located along the contact between the lower and upper plates and inside the

6   *A. Regorda* et al.

(a) Active oceanic subduction phase
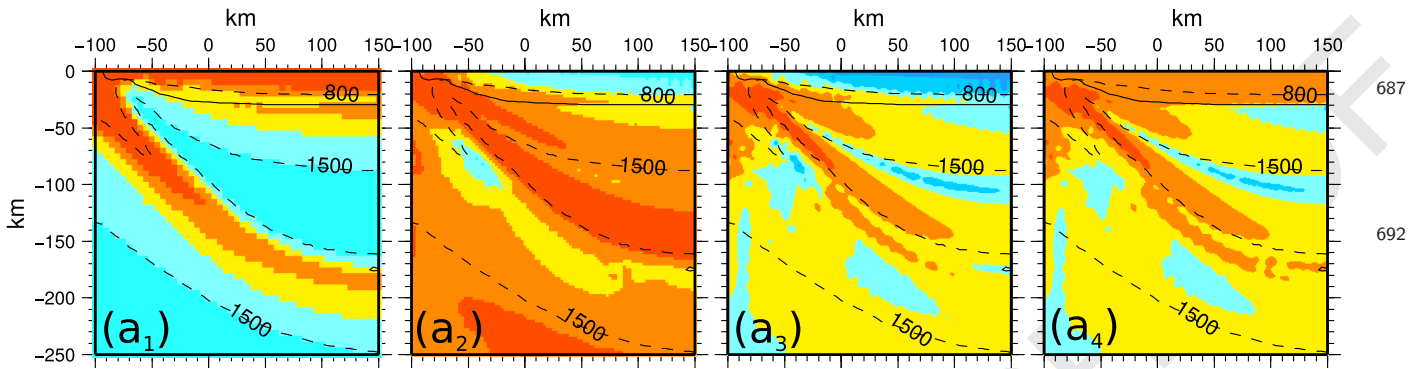
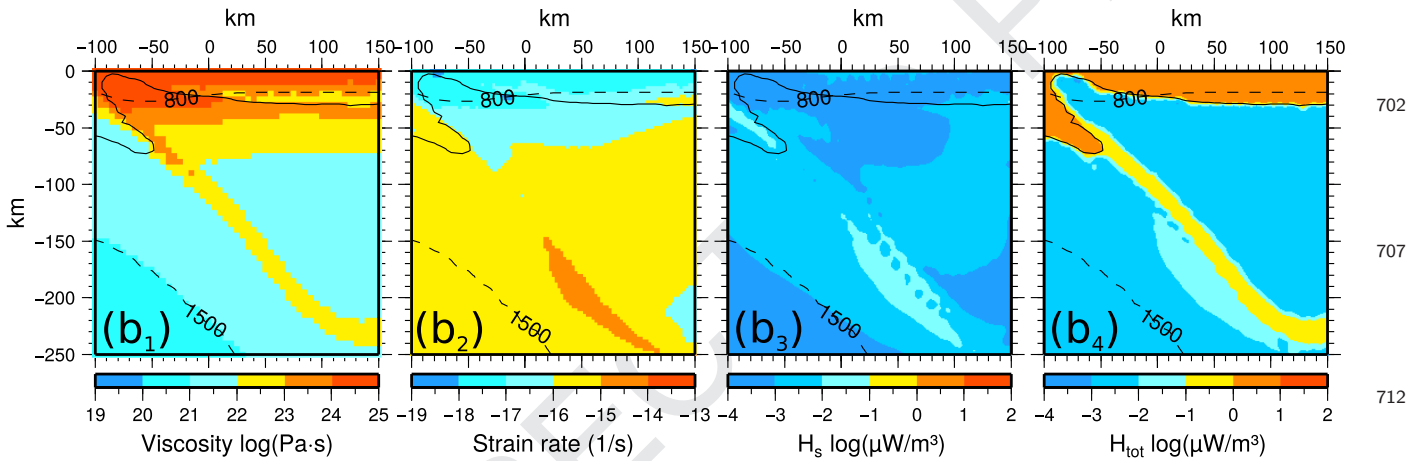## (b) Post-collisional phase

Figure 2. Distribution of the effective viscosity (a_1 and b_1), strain rate (a_2 and b_2), energy produced by shear heating (a_3 and b_3) and total energy (a_4 and b_4) predicted by model SH.5 at 10.5 Ma after the beginning of the active oceanic subduction phase (a) and at the end of the post-collisional phase (b). The dashed black lines indicate the 800 and 1500 K isotherms. The solid black lines indicate the base of the continental crust.

low-viscosity hydrated area (Fig. 4a_2). In contrast, the upper plate is characterized by strain rates of less than 10^{-16} s^{-1} at 150 km away from the trench (Fig. 4a_2). As observed in the REF models, the subducted lithosphere is colder for higher velocities of subduction and colder sections of the slab reach greater depths.

For at least the first 10 Ma of the post-collisional evolution, short-wavelength convective cells persist in the wedge area because of the significant extension of the hydrated domain (insets in Fig. 3b_1). Subsequently, they quickly vanish as the hydrated area disappears (Fig. 3b_2). Over longer times, the MH models undergo the same dynamics observed in the REF models that present a decrease in the slab dip, although the occurrence of recycled oceanic and continental crustal material in the mantle wedge determines the doubling of the crust at the end of the post-collisional phase (Fig. 3b_2). In addition to the general warming of the system because of the thermal re-equilibration that occurs during the post-collisional phase, the doubling in the thickness of the crust causes additional warming in the subduction complex compared with the REF models (see the isotherm 800 K Fig. 4b) because of the large amount of radiogenic energy (Fig. 4b_3). This new thermal field influences the viscosity and the strain rate, which show significantly different trends in both the wedge area and the subducted lithosphere with respect to the subduction phase (Figs 4b_1 and b$_2$). Specifically, the viscosity decreases in the interior of the subducted lithosphere and increases in the wedge area by up to three orders of magnitude (Fig. 4b_1), whereas the strain rate decreases in the entire domain by at least

three orders of magnitude because of the general velocity decrease (Fig. 4b_2) and small spatial gradients caused by crust–mantle compositional variations.

3.1.3 Effect of both shear heating and mantle hydration (SH+MH models)

The simultaneous occurrence of shear heating and mantle hydration (SH+MH models) significantly modifies the large-scale thermomechanics of the system, with respect to REF model, throughout the active oceanic subduction phase. The magnitude of convective flows decreases and the slab dip reduces (Fig. 5a) with respect to REF models (Fig. A1a). As for the SH models, a warming of the slab occurs with respect to the MH models (see the configuration of the 1500 K isotherm and the shallower maximum depth reached by the 800 K isotherm in Fig. 6a with respect to Fig. 4a), and the temperature of the mantle wedge increases, which produces a lower extension of the hydrated domain.

The total energy in the dry mantle of the SH+MH models (Fig. 6a_4) can be up to four orders of magnitude higher than that of the MH models (Fig. 4a_3), although it is similar to that predicted by SH models because of the large amount of energy produced by shear heating (Fig. 6a_3). However, the total energy in the hydrated area differs by less than one order of magnitude, because the low viscosity produced by hydration limits the energy produced by shear

(a) Active oceanic subduction phase

(b) Post-collisional phase

Continental
crust (UP)

Continental
crust (LP)

Oceanic
upper crust

Oceanic
lower crust

Hydrated area
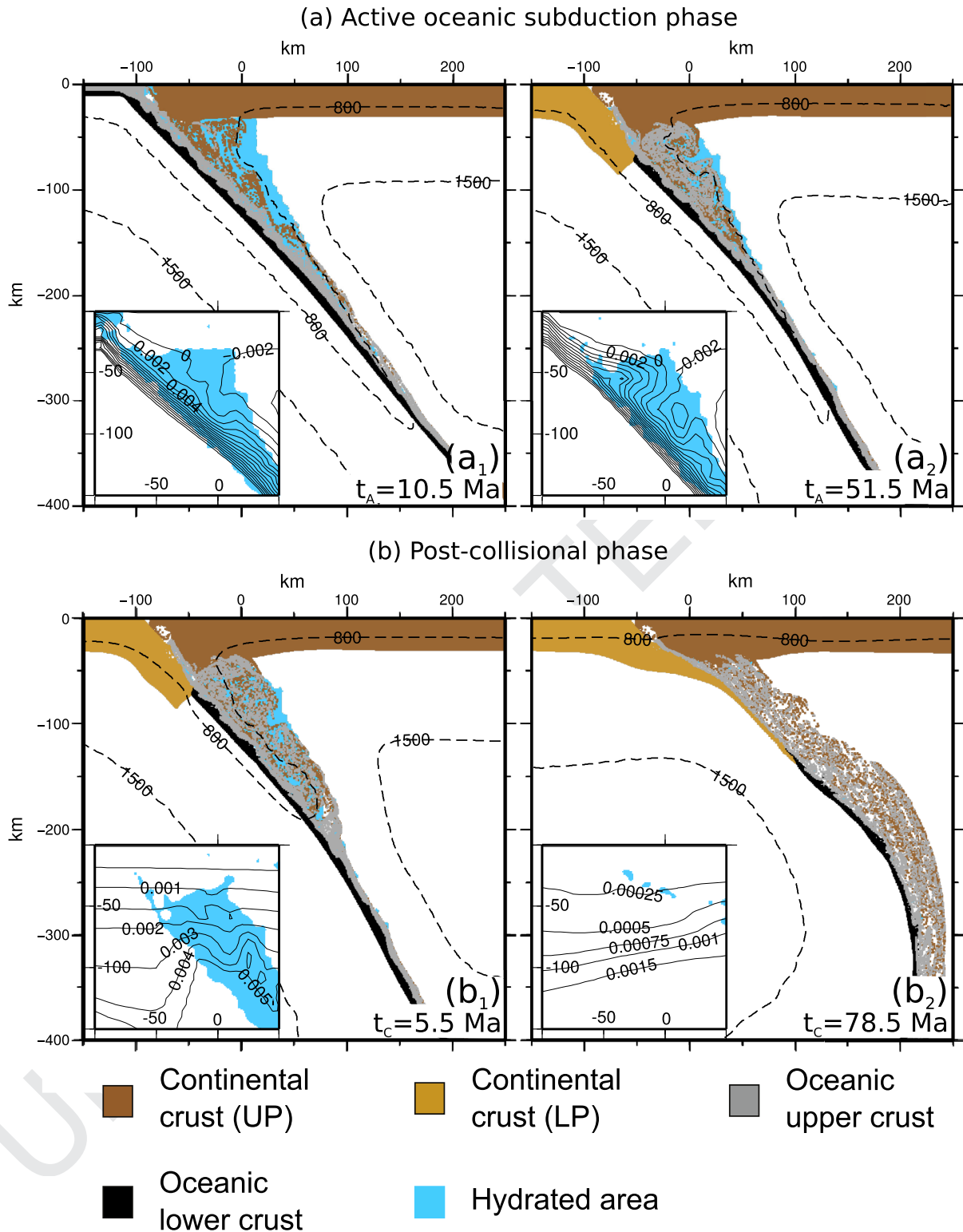
Figure 3. Isotherms 800 and 1500 K (dashed black lines) and streamline patterns (solid black lines in the insets) in the surrounding of the wedge area for model MH.5 at different times during the active oceanic subduction phase (a) and the post-collisional phase (b). t_A indicates times from the beginning of the active oceanic subduction phase; t_C indicates times from the beginning of the post-collisional phase. Numbers on streamlines are indexes of the intensity of the flow. UP stands for upper plate; LP stands for lower plate.

heating (approximately two to three orders of magnitude lower than in the dry mantle). Therefore, the increase in temperature driven by the shear heating in a hydrated system is less than that predicted by models without hydration (SH models). As predicted in the REF

models, velocity variations affect the temperature inside the slab. In fact, higher subduction velocities correspond to lower temperatures and lower slab dips (Figs $7a_1$ and b_1). Finally, similarly to that observed in the MH models, short-wavelength convective cells

(a) Active oceanic subduction phase
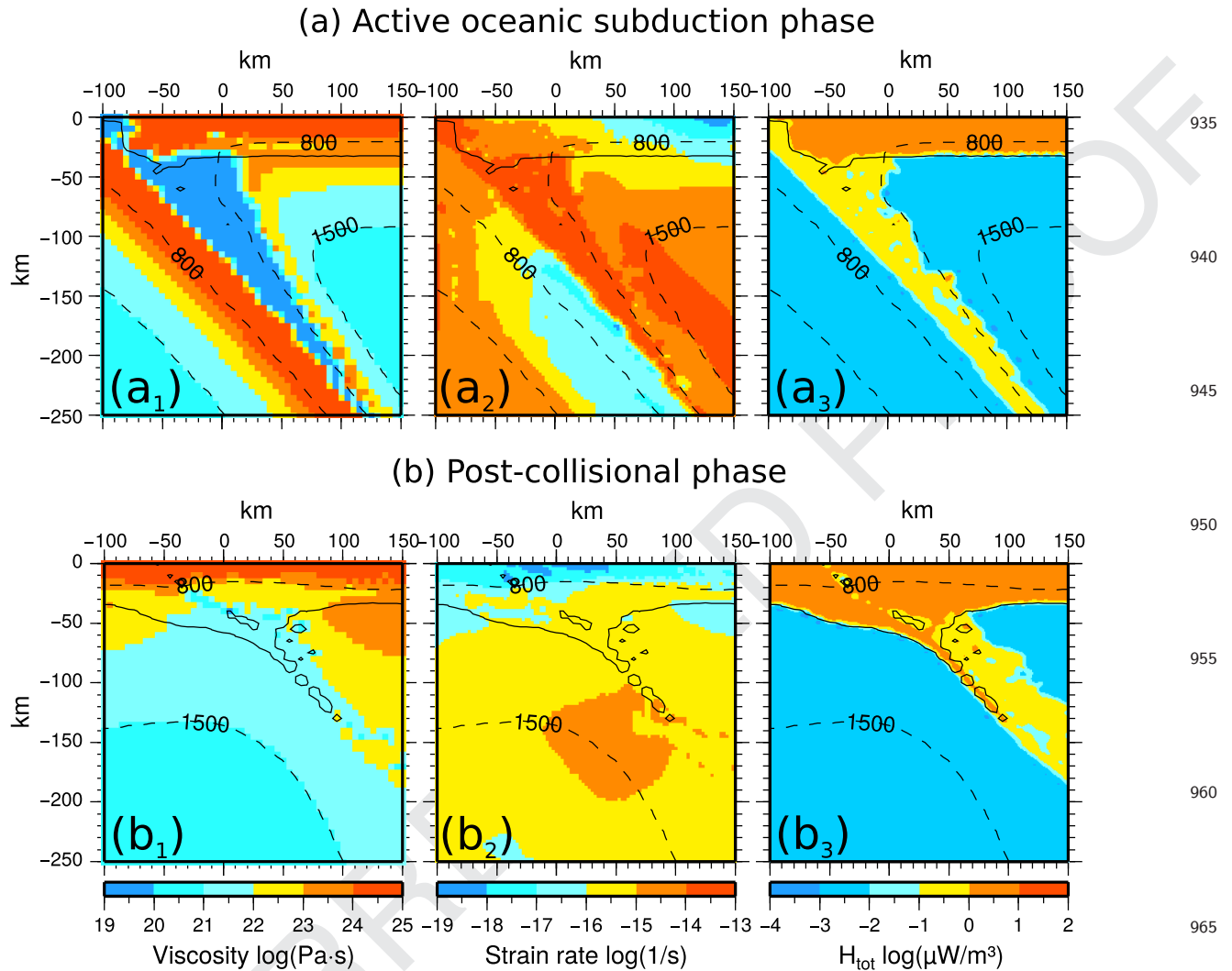
(b) Post-collisional phase

Figure 4. Distribution of the effective viscosity (a_1 and b_1), strain rate (a_2 and b_2) and total energy (a_3 and b_3) predicted by model MH.5 at 10.5 Ma after the beginning of the active oceanic subduction phase (a) and at the end of the post-collisional phase (b). The dashed black lines indicate the 800 and 1500 K isotherms. The solid black lines indicate the base of the continental crust.

active, producing the recycling of both continental and oceanic crustal material (insets in Figs $7a_1$ and b_1).

During the post-collisional phase, the thermomechanical evolution of the SH+MH models (Fig. 5b) is comparable to that of the MH models. A peculiar feature of the SH+MH models is that, during the post-collisional phase, slices of subducted crust can separate from the slab and rise to shallower depths (Figs $7a_2$ and b_2), thereby widening the area that is occupied by recycled crustal material in the supra-subductive mantle.

3.2 Evolution of the hydrated area

Here, we discuss the evolution of the hydrated area as a function of the subduction velocity for MH and SH+MH models. A more detailed and quantitative description of both similarities and differences between the two models is in Appendix C.

We distinguish between main and secondary hydrated areas. The main hydrated area is identified by a wide triangular domain, delimited at the base by both the top of the lower oceanic crust, and a single life cycle that lasts for tens Ma. Its evolution is characterized

by an initial phase of rapid growth, an intermediate phase with a nearly constant extent, and a final phase of rapid decrease (dashed lines in Fig. 8). The secondary, smaller, hydrated areas develop at the margin of the main hydrated area and persist for shorter time periods.

3.2.1 MH models

The hydration starts within 1 Ma after the beginning of the active oceanic subduction phase (continuous lines in Fig. 8a) and continues over a period that decreases with increasing prescribed velocity. The velocity of subduction also influences the growth rate, the maximum extension and the variation in time of the dimension of the hydrated areas, because of the strong relation between velocity and thermal fields. In particular, during the early stages of the active oceanic subduction, slower velocities correspond to both lower growth rate and smaller hydrated areas. During the advanced stages of active oceanic subduction, since the predicted thermal field in the wedge area is mainly controlled by the mantle flow, which is more intense in model MH.8 than in model MH.3, model MH.3 undergoes a

(a) Active oceanic subduction phase
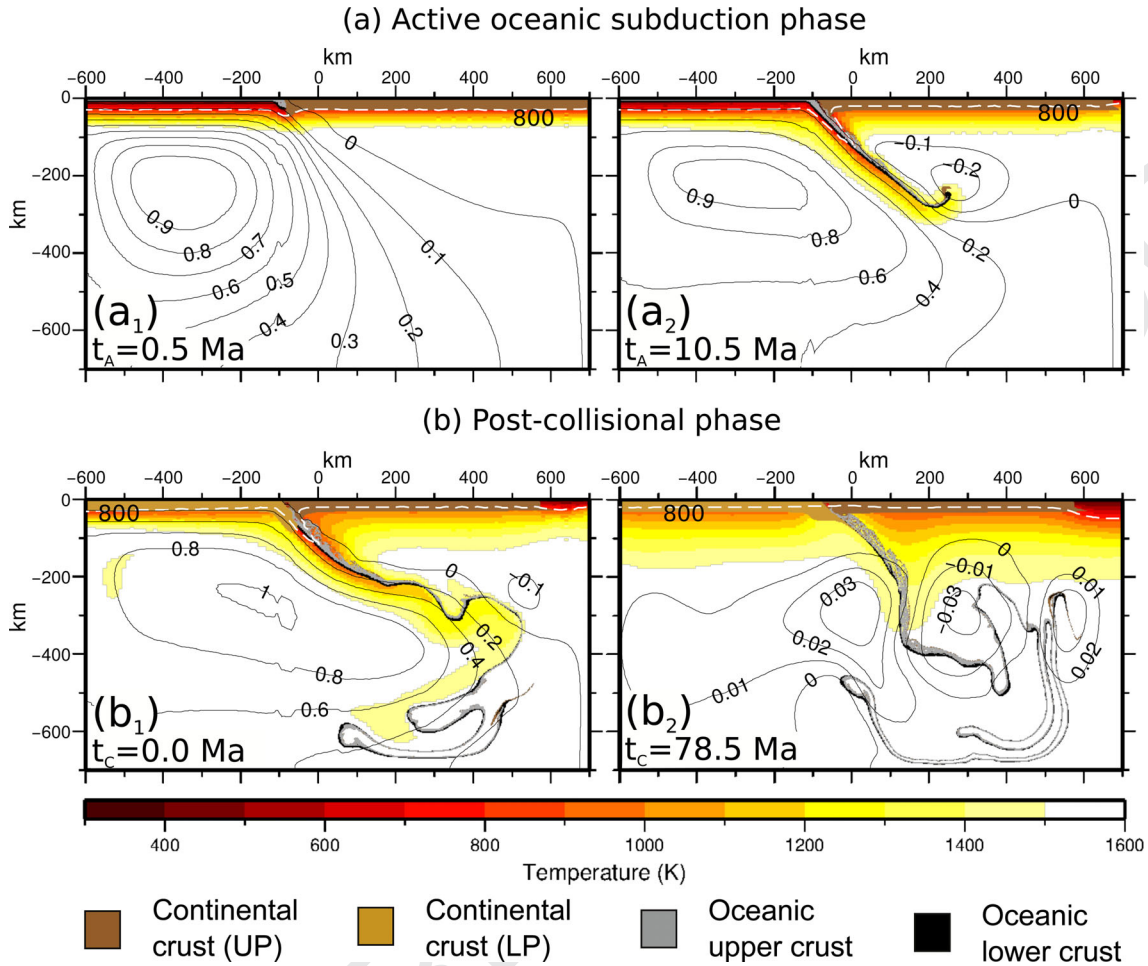

(b) Post-collisional phase

Figure 5. Large-scale temperature field (colours) and streamline patterns (solid black lines) predicted by model SH+MH.5 at different times during the active oceanic subduction phase (a) and the post-collisional phase (b). t_A indicates times from the beginning of the active oceanic subduction phase; t_C indicates times from the beginning of the post-collisional phase. The dashed white lines indicate the 800 K isotherm. Numbers on streamlines are indexes of the intensity of the flow. UP stands for upper plate; LP stands for lower plate.

Active oceanic subduction phase
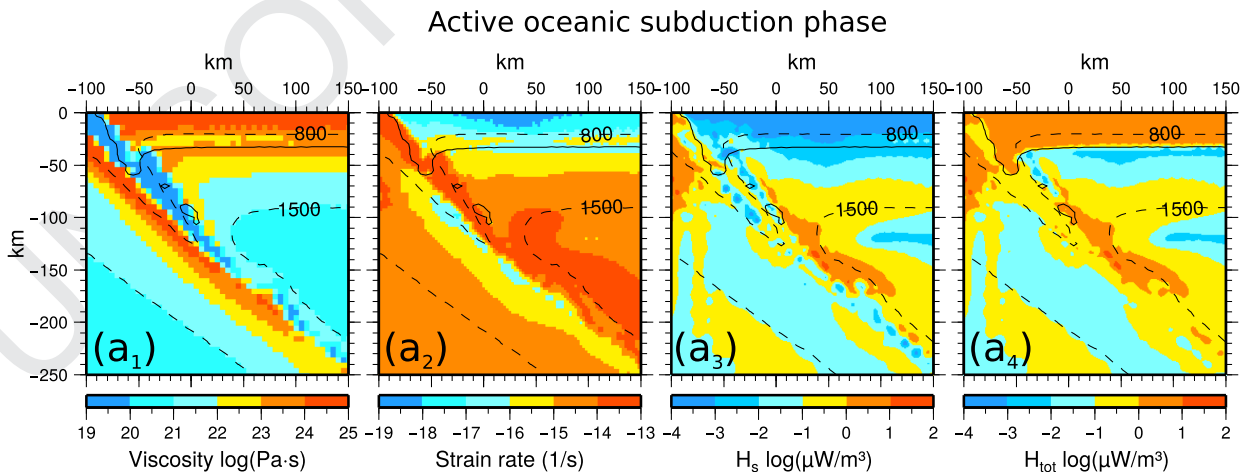
Figure 6. Distribution of the effective viscosity (a_1), strain rate (a_2), energy produced by shear heating (a_3) and total energy (a_4) predicted by model SH+MH.5 at 10.5 Ma after the beginning of active oceanic subduction phase. The dashed black lines indicate the 800 and 1500 K isotherms. The solid black lines indicate the base of the continental crust.

continuous cooling throughout the active oceanic subduction phase with a gradual increase in the extension of the hydrated area (red line in Fig. 8a) and two maxima can be identified ($P_{3.1}$ and $P_{3.2}$ In Fig. 8a). Differently, models MH.5 and MH.8 are characterized by

an initial cooling phase, until a maximum in the extension of the hydrated area at 10–15 Ma ($P_{5.1}$ and $P_{8.1}$ in Fig. 8a, respectively), and a successive rapid warming, which produces a significant decrease in the extension (continuous green and blue lines in Fig. 8a,
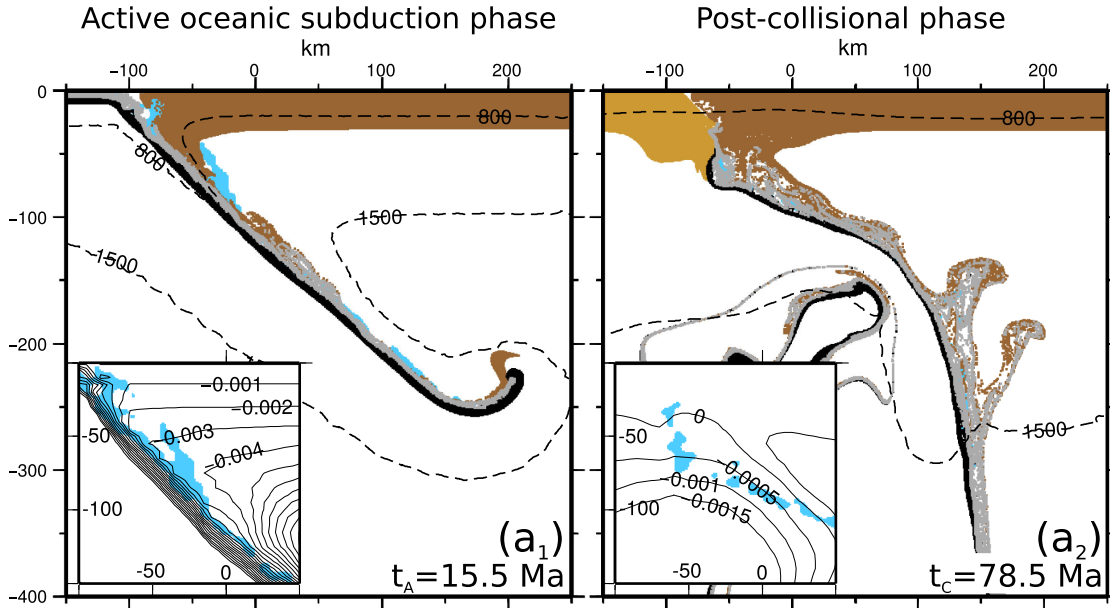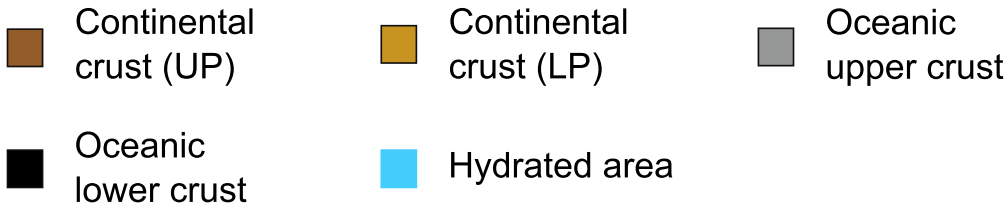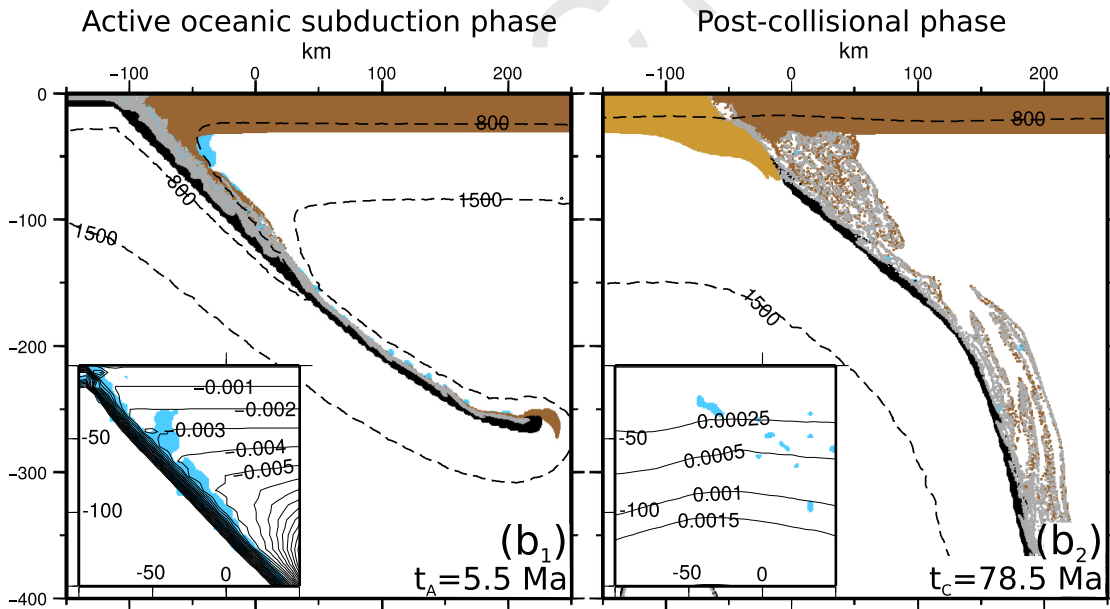
Figure 7. Isotherms 800 and 1500 K (dashed black lines) and streamline patterns (solid black lines in the insets) in the surrounding of the wedge area for models SH+MH.3 (a) and SH+MH.8 (b) at different times during the active oceanic subduction phase (panels a_1 and b_1) and the post-collisional phase (panels a_2 and b_2). t_A indicates times from the beginning of the active oceanic subduction phase; t_C indicates times from the beginning of the post-collisional phase. Numbers on streamlines are indexes of the intensity of the flow. Different ages have been chosen in order to compare similar evolutionary stages of oceanic subduction for different velocities, such as similar depths reached by slab. UP stands for upper plate; LP stands for lower plate.
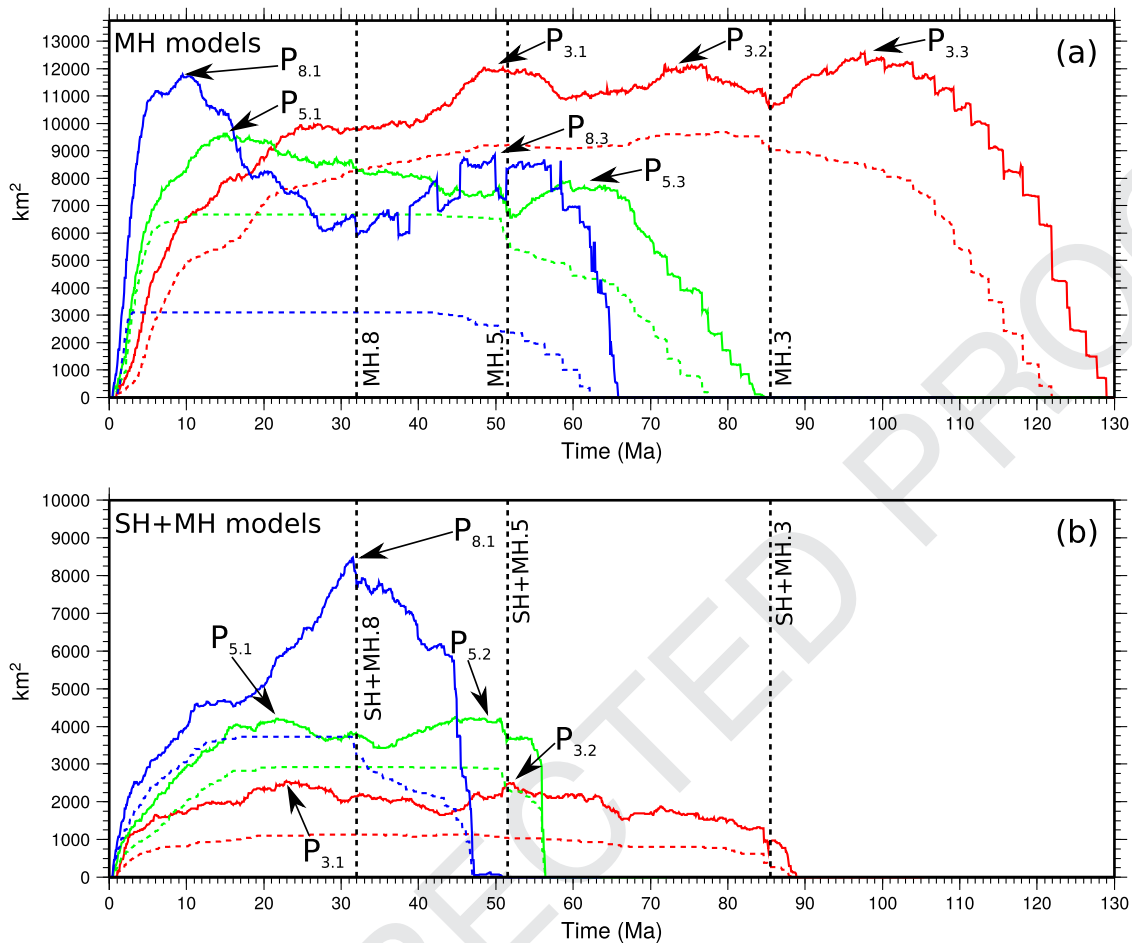
Figure 8. Variations in time of the dimension of the total (continuous lines) and main (dashed line) hydrated area for MH (panel a) and SH+MH (panel b) models. Red, green and blue lines refer to convergent velocities of 3, 5 and 8 cm yr^{-1}, respectively. The vertical dashed lines indicate the time when the continental collision occurs for the different models. $P_{3.i}$, $P_{5.i}$ and $P_{8.i}$ indicate the maxima of the extension of the hydrated area for convergent velocities of 3, 5 and 8 cm yr^{-1}, respectively.

respectively). During the active oceanic subduction phase, for all MH models a first maximum in the extension of the hydrated area is reached several tens Ma before continental collision.

For what concerns the sole main hydrated area, it persists for a minimum of 40 Ma for all MH models. The dimension of the main hydrated area increases with decreasing velocity during the active oceanic subduction phase (dashed red, green and blue lines in Fig. 8a and grey squares in Fig. A4) because the thermal field in the internal portion of the wedge is not influenced by the mantle flow but it depends only on the temperature inside the slab, which is lower for higher velocities of subduction.

The secondary hydrated areas are mostly located along the external and deepest portions of the main hydrated area (coloured squares in Fig. A4). Their occurrence and locations are controlled by periodic fluctuations in the local thermal state. Two main episodes of growth of secondary hydrated areas occur in the low velocity model (MH.3), while only one episode occurs in intermediate and high velocity models (MH.5 and MH.8).

At the collision, the hydrated area decreases abruptly by several hundreds of square kilometres (red, green and blue lines in Fig. 8a). This decrease follows the partial subduction of the continental crust of the lower plate, which confines the low viscosity hydrated channel between the upper plate and the subducting lithosphere. An important change in the boundaries of the hydrated area occurs after the

collision when the growth of secondary hydrated areas results in an increase of the extension of the hydrated area of few thousands of square kilometres ($P_{3.3}$, $P_{5.3}$ and $P_{8.3}$ in Fig. 8a).

3.2.2 SH+MH models

We here enlighten the sole main differences in the evolution of SH+MH models with respect to MH models. In SH+MH models the maximum extent of the hydrated areas increase with increasing prescribed velocity during the whole active oceanic subduction phase (continuous lines in Fig. 8b), consistently with the lower temperatures in the mantle wedge predicted for intermediate and high prescribed velocities. Furthermore, the warmer thermal state determines hydrated areas significantly less extended than in MH models. A peculiar feature of the high velocity model (SH+MH.8) is the continuous enlargement of the hydrated area, until a maximum reached at the continental collision ($P_{8.1}$ in Fig. 8b). The extension of the hydrated area of the SH+MH.8 model shows only one maximum and this is related to the more stable thermal field that characterizes the active oceanic subduction phase of the high velocity model.

The main hydrated areas persist for shorter periods (30 Ma; dashed red, green and blue lines in Fig. 8b and grey squares in

Fig. A5) and extend to lower depths than in MH models. With respect to MH models, two main episodes of growth of secondary hydrated areas occur for both low and intermediate velocity models ($P_{3.1}$, $P_{5.1}$, $P_{3.2}$ and $P_{5.2}$ in Fig. 8b).

During the early stages of the post-collisional phase, the hydrated area of all models gradually decreases, with a longer duration of hydration for the high velocity model (SH+MH.8, blue line in Fig. 8b) due to the lower temperatures that characterize the wedge area. However, the general warmer thermal state of SH+MH models prevents the occurrence of a maximum in the extension of the hydrated area after the continental collision.

3.3 Predicted *P–T* conditions and metamorphic gradients

Here, we discuss the different pressure (*P*) and temperature (*T*) conditions recorded by markers of oceanic and continental crust for models that have mantle hydration, without (MH) and with (SH+MH models) shear heating. For markers that have recorded a maximum pressure higher than their final pressure, such as they can be considered exhumed, we analysed the *P–T* conditions at maximum pressure (P_{max}–*T*) and maximum temperature (*P*–T_{max}). Two *P*- and *T*-peak conditions are distinguished: one that characterizes the active oceanic subduction phase (P_{maxA} and T_{maxA}) and one that characterizes the post-collisional phase (P_{maxC} and T_{maxC}). Areas of subducted materials are calculated as the unit area of a single a marker (0.25 km^2) multiplied by the number of markers.

Metamorphic facies series with high *P/T* ratios are generally associated with *P–T* conditions that are peculiar to oceanic subduction (e.g. Spear 1993; Kornprobst 2002; Nicollet 2010). This type of metamorphic facies association, which is deduced from regional scale metamorphic settings inferred from fieldwork (Miyashiro 1961; Ernst 1973), is referred to as either a Franciscan or a Sanbagawa metamorphic sequence. The geological literature indicates that Barrovian or Dalradian metamorphic series, characterized by intermediate *P/T* ratios, develop during continental collisions (England & Richardson 1977; Thompson 1981; England & Thompson 1984; Thompson & England 1984; Spear 1993). Metamorphic facies series characterized by low *P/T* ratios (Abukuma or Buchan-type metamorphism) have generally been associated with abnormally high geothermal gradients, such as those detected in arc regions. Miyashiro (1961, 1973) developed the idea of paired metamorphic belts based on the juxtaposition of orogenic crustal sections that are characterized by Sanbagawa- and Abukuma-type metamorphic facies series.

3.3.1 *MH models*

An analysis of the P_{maxA}–*T* trend indicates that large amounts of continental crust from the upper plate (corresponding to areas of approximately 6700, 8000 and 7000 km^2 for subduction rates of 3, 5 and 8 cm yr^{-1}, respectively) record P_{maxA}–*T* conditions with intermediate *P/T* ratios (Barrovian metamorphism), which are warmer than those prescribed by the assumed initial continental geotherm (Fig. 9a). These markers were never subducted at high depths but they were displaced from the external portion of the upper plate toward the wedge, recording the P_{maxA} during the first 10 Ma of evolution of the active oceanic subduction phase (Fig. 9b).

A smaller amount of both oceanic and continental material (ranging from 2000 km^2 for a subduction rate of 3 cm yr^{-1} to 1000 km^2 for a subduction rate of 8 cm yr^{-1}) records high *P/T* ratios (Franciscan metamorphism), with P_{maxA} values reaching up to 3 GPa and *T*

reaching up to 800 K during sinking (Figs 9a and b). The *P–T* conditions are colder than the assumed initial continental geotherms, and these materials record the P_{maxA} values during the entire active oceanic subduction phase (Fig. 9b). Similar conclusions can be obtained by observing the distribution of the *P–*T_{maxA} predictions (Figs 9c and d) for low, intermediate and high *P/T* ratios. Markers with intermediate *P/T* ratios record the thermal peak during the entire active oceanic subduction phase, whereas markers with high *P/T* ratios record the thermal peak during late stages of the oceanic subduction (Fig. 9d).

Fig. 10(a) show the predicted *P–T* conditions recorded by all the crustal markers, both oceanic and continental, at different times during the entire active oceanic subduction phase. The global thermal configuration of the system does not change significantly with time (compare panels a_1, a_2 and a_3 of Fig. 10). Although the minimal temperatures for *P* > 1.5 GPa increase by approximately 100 K when the continental markers of the lower plate are subducted up to approximately 2.5 GPa (Fig. 10a_3). The non-subducted markers of the upper plate (*P*< 0.8 GPa) have intermediate *P/T* ratios, and the subducted markers of both the upper and lower plates (*P* > 0.8 GPa) have high *P/T* ratios. These results indicate that intermediate *P/T* ratios can co-exist with high *P/T* ratios within an subduction complex (Fig. 10a).

During the post-collisional phase, the P_{maxC}–*T* values of the continental markers (Fig. 11a) shift from the Franciscan to Barrovian fields from the beginning (red colours in Fig. 11b) to the end (blue colours in Fig. 11b) of the post-collisional phase. The maximum temperature for the P_{maxC}–*T* values is 1300 K for models MH.3 and MH.5 and 1200 K for model MH.8.

The subduction velocities influence the distribution of the *P–*T_{maxC} values during the post-collisional phase only. For intermediate velocities (model MH.5), the markers are distributed along a narrow curved area with a maximum temperature of approximately 1400 K at approximately 1.5 GPa (Figs 11c and d). These markers plot in the Barrovian field with the exception of markers with *P* > 2 GPa, which are characterized by Franciscan-type *P/T* ratios. Oceanic markers only occur at pressures higher than 0.5 GPa (Fig. 11c). For low velocities (model MH.3), the markers that record *P* > 0.5 GPa have temperatures that range between 800 K and 1300 K, and they are characterized by intermediate to high *P/T* ratios (Fig. 12a). Finally, for high velocities (model MH.8), continental markers from the lower plate only appear at *P* < 2 GPa and lie within a narrow curved area with a maximum temperature of 1200 K at approximately 2 GPa. Continental markers that belong to the upper plate and upper oceanic markers record temperatures between 800 K and 1300 K and pressures of up to 3 GPa. The most of the markers (corresponding to an area of approximately 2000 km^2) record intermediate *P/T* ratios except for a few markers with pressures greater than 1.5 GPa that exhibit high *P/T* ratios (Fig. 12b).

After the continental collision, all MH models show a progressive increase of temperature with time (Fig. 10b); thus, T_{max} recorded during the post-collisional phase are recorded at the end of the evolution (Fig. 11d). All markers record intermediate to high *P/T* ratios with a migration toward *P–T* conditions that are warmer than the assumed initial continental geotherm (Figs 11c and d).

3.3.2 *SH+MH models*

During subduction, all SH+MH models show P_{maxA}–*T* values characterized by intermediate and high *P/T* ratios (Figs 13a and b). The amount of markers with P_{maxA}–*T* values characterized by
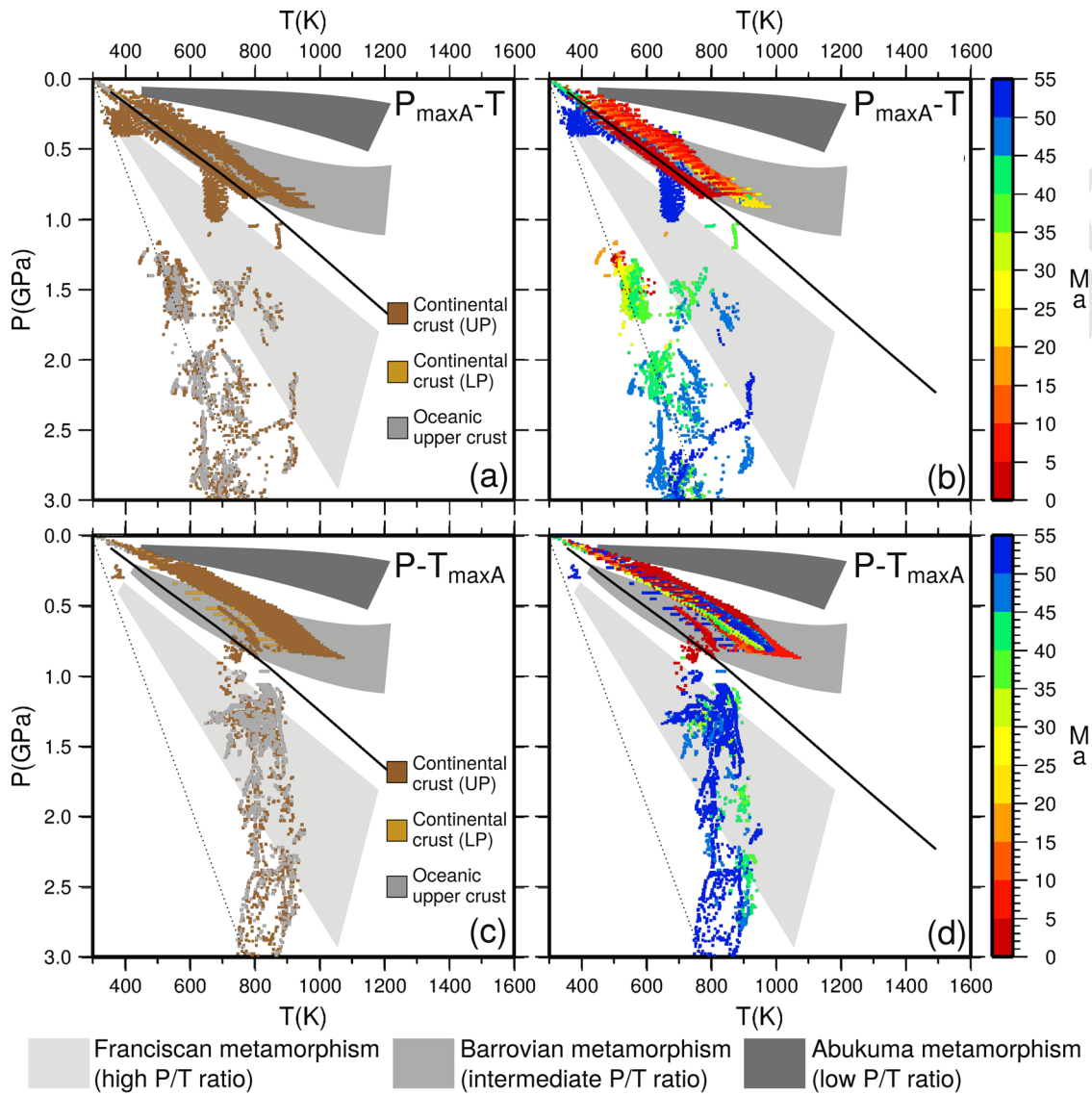
Figure 9. Predicted $P_{maxA}-T$ (panels a and b) and $P-T_{maxA}$ (panels c and d) distributions of exhumed markers for the MH.5 model during the active oceanic subduction phase. In panels b and d, the markers are coloured according to the age at which P_{maxA} and T_{maxA} are reached. The thick black lines represent the unperturbed continental geotherm. The dashed line indicates conditions not realized on Earth. UP stands for upper plate; LP stands for lower plate.

high P/T ratios depends on the prescribed subduction velocity. In particular, model SH+MH.3 shows only a small amount of markers (corresponding to a total area of approximately 100 km²) with high P/T ratios, whereas models SH+MH.5 and SH+MH.8 show a remarkably large amount of oceanic and continental markers (corresponding to total areas of approximately 1400 and 1000 km², respectively). These markers exhibit $P > 1.5$ GPa with temperatures between 600 and 1000 K for model SH+MH.5 (Fig. 13a) and between 500 and 1000 K for model SH+MH.8, and they record the pressure peak throughout the whole subduction (Fig. 13b).

The $P-T_{maxA}$ distribution of model SH+MH.3 shows similar features to the $P_{maxA}-T$ distribution with a narrower range of temperatures (approximately 50 K at approximately 1000 K) and pressures between 2.3 and 2.7 GPa. In contrast, in model SH+MH.5 (and model SH+MH.8, which is not shown in figures) markers cluster at $P-T_{maxA}$ values greater than 1 GPa in two groups that depend on the time at which their thermal peaks are recorded (Figs 13c and d). One group, which is composed of both continental and oceanic markers (Fig. 13c) with maximum temperatures of approximately 1000 K

and high P/T ratios, records the thermal peak during the second half of the active oceanic subduction phase (Fig. 13d). The second group, which is composed of only continental crustal markers of the upper plate (Fig. 13c) with temperatures between 1000 and 1300 K and pressures between 1.3 and 2 GPa, records the thermal peaks during the first 5 Ma of active oceanic subduction phase (Fig. 13d). The P/T ratios of the second group are lower than the P/T ratios of the first group and similar to the assumed initial continental geotherm. As in the MH models, the thermal state remains stationary during the entire active oceanic subduction phase, and intermediate and high P/T ratios may co-exist in the subduction complex.

During the post-collisional phase, the distribution of the $P_{maxC}-T$ and $P-T_{maxC}$ values is similar to that of the MH models and include a wide range of temperatures for the $P_{maxC}-T$ values (approximately 500 K at 1.5 GPa) and a narrow range for the $P-T_{maxC}$ values (approximately 100 K at every depth). The $P_{maxC}-T$ values exhibit intermediate to high P/T ratios, whereas the $P-T_{maxC}$ values are mainly characterized by intermediate P/T ratios (data with high P/T ratios only occur above 2 GPa). As in the MH models, high
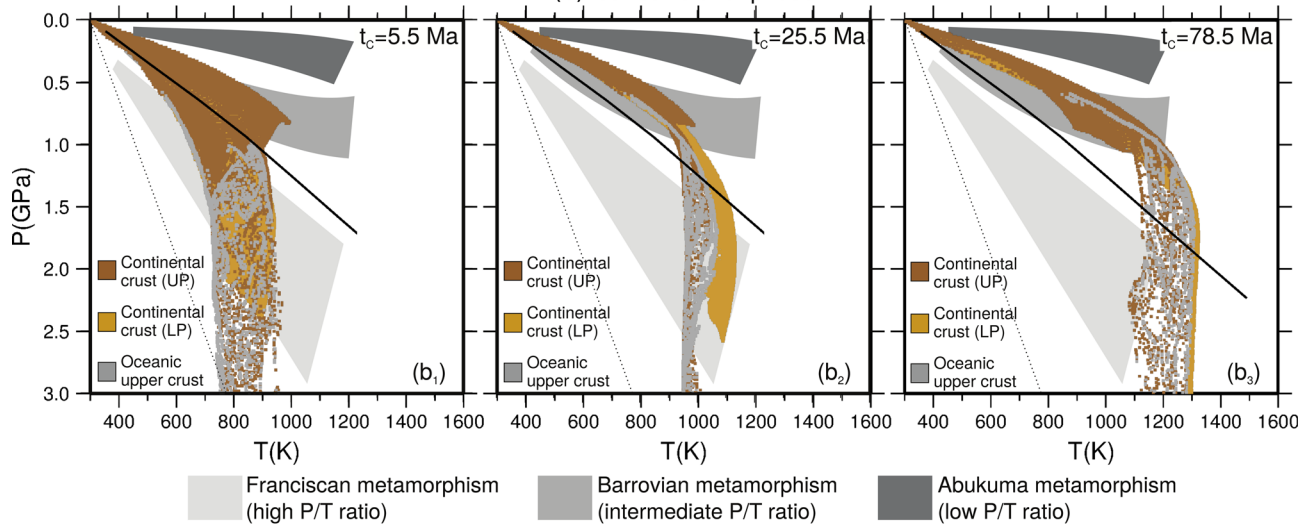
Figure 10. Predicted P–T conditions recorded by all markers of the MH.5 model at different times during the active oceanic subduction phase (a) and the post-collisional phase (b). t_A indicates times from the beginning of the active oceanic subduction phase; t_C indicates times from the beginning of the post-collisional phase. The thick black lines represent the unperturbed continental geotherm. The dashed line indicates conditions not realized on Earth. UP stands for upper plate; LP stands for lower plate.

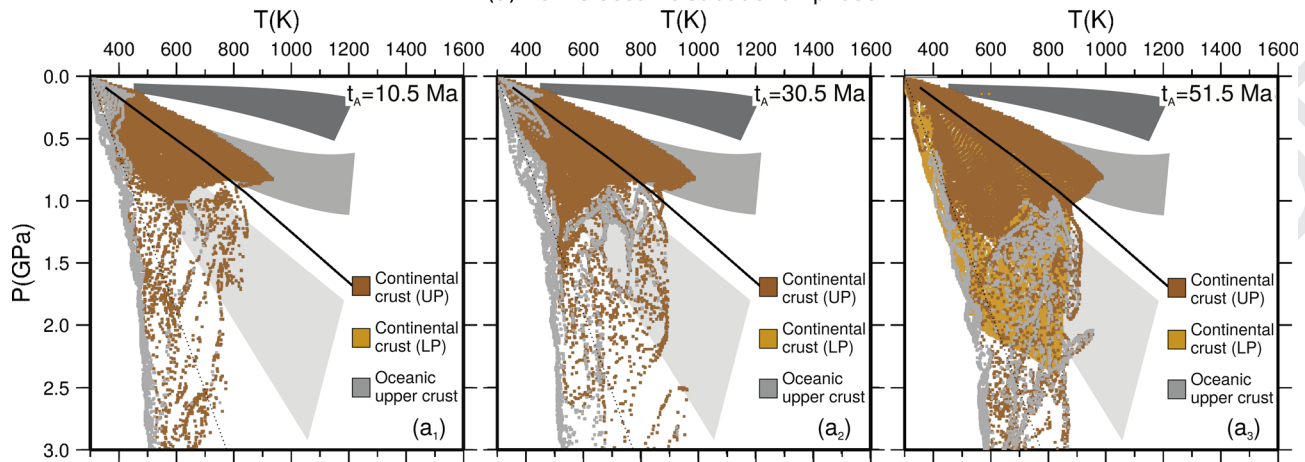P/T ratios for the P_{maxC} values are recorded until 10 Ma of post-collisional evolution, whereas the T_{maxC} values are recorded during the last stages of the post-collisional evolution.

In the SH+MH models, a progressive increase in temperature occurs throughout the entire system during the post-collisional phase, although the warming trend is higher than that in the MH models, as expected. Similar to the MH models, the majority of the markers show intermediate P/T ratios at the end of the evolution, whereas high and intermediate P/T ratios co-exist during the early stages of the post-collisional phase.

4 DISCUSSION

Our results indicate that in all models, the dynamics of the ocean/continent subduction system are characterized by an intense large-scale mantle flow underneath the overriding continental plate, as already observed by many authors (e.g. Andrews & Sleep 1974; Uyeda & Kanamori 1979; Davies & Stevenson 1992; Peacock 1996; Stern 1998; Gerya *et al.* 2002). This flow both erodes continental material from the base of the upper plate and increases the

temperature in the internal portion of the wedge. Furthermore, the REF models (Appendix B) lack a short-wavelength convective flow in the mantle wedge area and show no evidence of the inclusion of recycled subducted material, which prevents exhumation during subduction (e.g. Marotta & Spalla 2007; Spalla & Marotta 2007). The temperature in the subducted lithosphere is colder for higher velocities of subduction because the slabs heats up by conduction and cold sections of the slab reach greater depths than if they were moving with a slower velocity. On the other hand, the corner flow is more intense for higher velocities of subduction, with consequent higher temperatures in the mantle wedge. If shear heating is included (SH models), a significant increase in temperature occurs in the mantle wedge and the subducting oceanic lithosphere, although the dynamics remains globally unchanged.

When mantle hydration is accounted in the absence of shear heating (MH models), small convective cells activate in the hydrated area from the early stages of subduction, thereby favouring the partial exhumation of buried oceanic and continental crust. This dynamics is compatible with that observed by previous authors (e.g. Ida 1983; Iwamori 1998; Billen & Gurnis 2001). Moreover, the hydrated area has a rather triangular shape as suggested by previous models

1746

1751

1756

1761

1766

1771

Figure 11. Predicted P_{maxC}–T (panels a and b) and P–T_{maxC} (panels c and d) distributions of exhumed markers for MH.5 model during the post-collisional phase. In panels (b) and (d), the markers are coloured according to the age at which P_{maxC} and T_{maxC} are reached. The thick black lines represent the unperturbed continental geotherm. The dashed line indicates conditions not realized on Earth. UP stands for upper plate; LP stands for lower plate.

1776

1803

1808

1813

1818

1823

1828

1833

1838

(Arcay *et al.* 2005; Hebert *et al.* 2009; Quinquis & Buiter 2014; Wilson *et al.* 2014). During the early stages of active oceanic subduction phase, higher subduction velocities correspond to larger hydrated areas because of the lower temperatures predicted inside the slab. However, during the mature stages of the subduction the temperature in the wedge is controlled by the large-scale mantle flow, which is more intense for higher velocities and causes an increase in temperature. Therefore, higher subduction velocities correspond to smaller hydrated areas. The hydration causes a decrease in temperature in the inner portion of the wedge compared to that of REF models because of the uplift of cold material from the subducted plate.

The introduction of shear heating in the hydrated models (SH+MH) causes a shallower subduction geometry, which is more evident for higher prescribed subduction velocities. The thermal state in the hydrated area is slightly influenced by the introduction of shear heating because the decrease in mantle viscosity is dominant over the increase in strain rate. Accordingly, radiogenic heat remains the principal source of internal energy. However, an increase in temperature in the external portion of the dry mantle wedge can be observed and the extension of the hydrated area subsequently decreases. In the SH+MH models, higher subduction velocities correspond to larger extensions of the hydrated area throughout the entire active oceanic subduction phase because, compared with the models with lower velocities, the model with fast velocities results in lower temperatures and larger areas in which the serpentine is stable.

The main hydrated area is characterized by an initial phase of rapid growth in size, an intermediate phase during which the extent remains almost constant, and a final phase of rapid decrease in the extension. Secondary smaller hydrated domains develop in different positions with respect to the main hydrated area and persist for shorter time periods. The occurrence and locations of the secondary hydrated areas are controlled by the periodic fluctuations in the thermal state that characterize the edges of the main hydrated area and determine the growth of both the external and deep

1781

1786

1791

1796

1843

1848

1853

1858
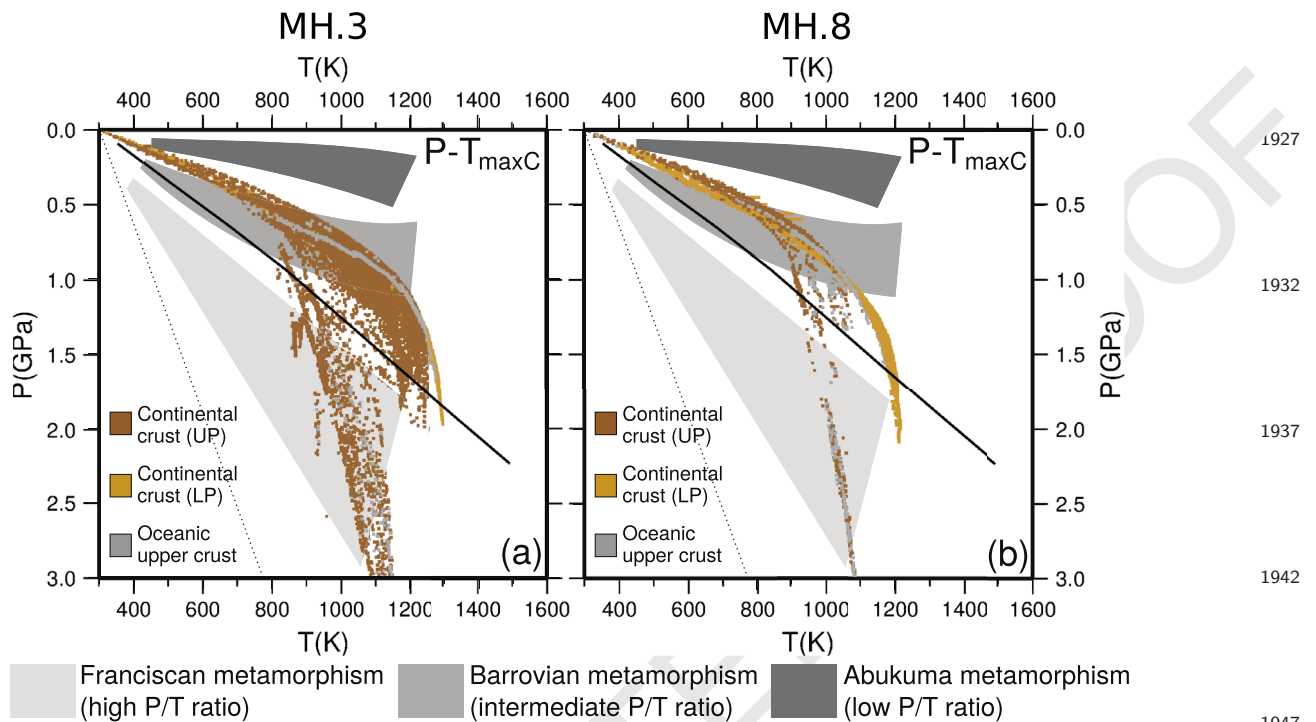
Figure 12. Predicted P–T_{maxC} and distributions of exhumed markers for the MH.3 model (panel a) and MH.8 model (panel b) during the post-collisional phase. The thick black lines represent the unperturbed continental geotherm. The dashed line indicates conditions not realized on Earth. UP stands for upper plate; LP stands for lower plate.

portions of the total hydrated areas. The more stable thermal field that characterizes the active oceanic subduction phase of the high velocity model generates only one maximum in the extension of the hydrated area.

At the continental collision, the hydrated area decreases abruptly in all models after the partial subduction of the continental crust of the lower plate, which confines the low viscosity hydrated channel between the upper plate and the subducting lithosphere. During the early stages of the post-collisional phase, the hydrated area of all models still gradually decreases. The occurrence of shear heating decreases the extension of the hydrated area as well as its duration after the collision because temperature in the area bordering the mantle wedge increases.

The small convective cells are active for approximately 10 Ma of post-collisional evolution. During the post-collisional phase, the large amount of recycled material in the wedge in the models MH and SH+MH produces a doubling of the crust, which increases the radiogenic decay and temperatures with respect to that of the SH models.

Our results suggest that the geodynamic significance of metamorphic gradients that are traditionally derived by 1-D models should be revised. Despite the peculiar significance that has been traditionally assigned to metamorphic facies series, our results show that contrasting P–T conditions, such as intermediate (Dalradian/Barrovian) to high P/T ratios (Franciscan/Sanbagawa), can occur simultaneously during the active oceanic subduction phase, which is demonstrated by the contrasting PT conditions (Franciscan or Barrovian) experienced by different crustal markers contemporaneously located in different regions of the subduction/collision system. In the MH and SH+MH models, markers that record Barrovian-type P_{maxA}–T conditions during early subduction have trajectories that indicate that they are carried by mantle flow from the bottom of

the continental crust of the upper plate toward the more internal and shallower portion of the mantle wedge. The markers that record Franciscan-type P_{maxA}–T conditions are exhumed by the activation of convective cells. The recycled crustal material is either tectonically sampled from the subducting plate or ablated by the upper plate in the mantle wedge.

The thermal state during the post-collisional phase remains comparable to that of the subduction phase until approximately 10 Ma of evolution, until small-scale convective cells deactivate and wedge dehydration occurs. Subsequently, the system progressively warms because of the thermal re-equilibration of the system and the high radiogenic energy localized in the doubled crust. The progressive warming of the system generates a thermal environment in which the markers primarily experience P–T conditions that are compatible with Barrovian- (or Dalradian-)type metamorphism at the end of the evolution, and the final thermal gradient is higher than the assumed initial continental geotherm. In all models, the highest T_{maxC} values are reached at the end of the evolution, whereas the markers attain their P_{maxC} values during the early stages of the gravitational evolution before the uplift of the subducted plate.

5 CONCLUSIONS

We have investigated the effects of shear heating and mantle hydration on the dynamics of the mantle wedge by means of a 2-D thermomechanical FE model of an ocean/continent subduction system characterized by different subduction velocities.

Our results indicate that:

(1) during the active oceanic subduction phase, although shear heating may induce a significantly warming of the subduction complex, the temperature increase is not sufficient to produce a
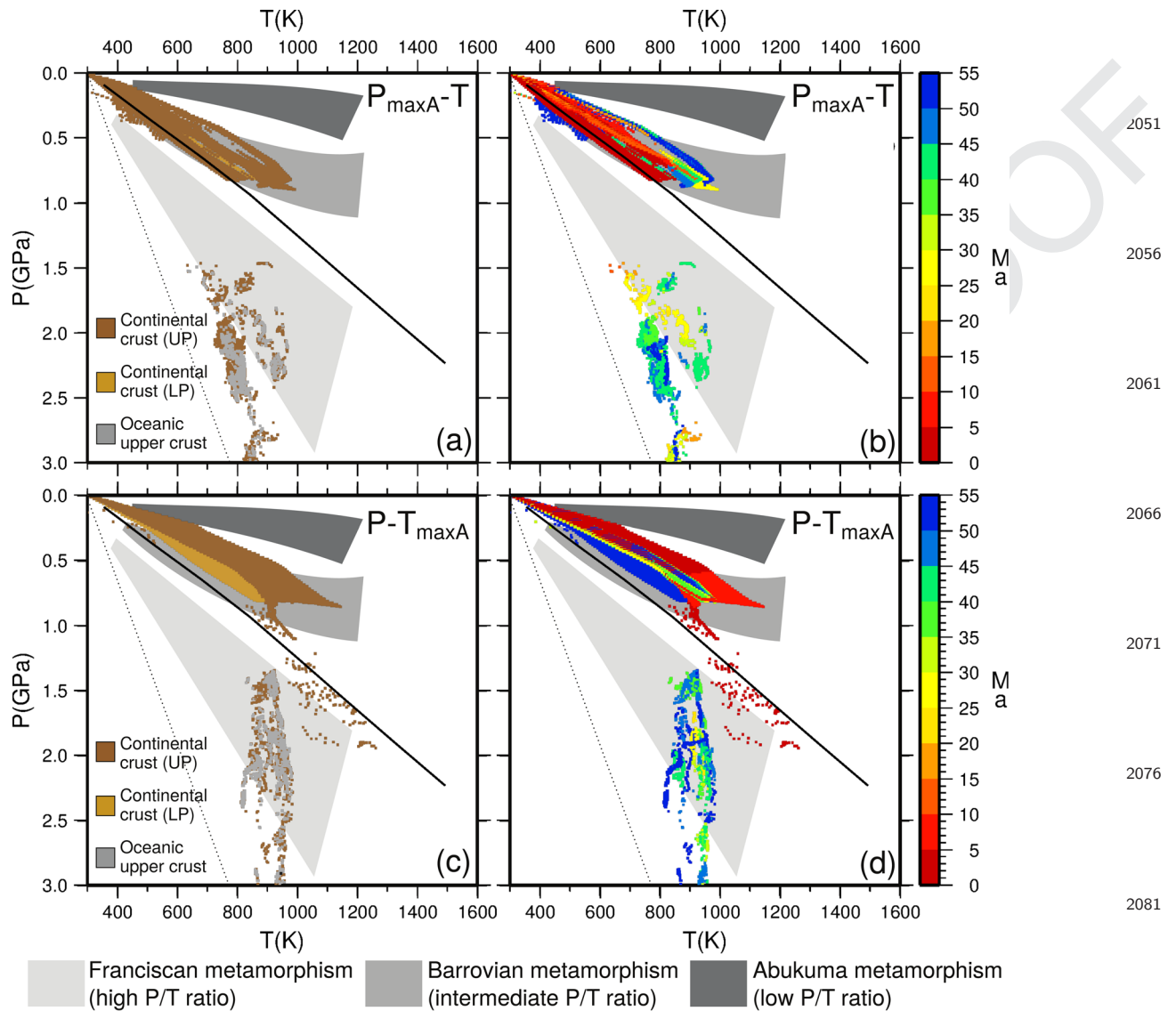
Figure 13. Predicted P_{maxA}–T (panels a and b) and P–T_{maxA} (panels c and d) distributions of exhumed markers for the SH+MH.5 model during the active oceanic subduction phase. In panels (b) and (d), the markers are coloured according to the age at which P_{maxA} and T_{maxA} are reached. The thick black lines represent the unperturbed continental geotherm. The dashed line indicates conditions not realized on Earth. UP stands for upper plate; LP stands for lower plate.

remarkable decrease in viscosity and the introduction of mantle hydration is necessary to activate of local convective flows in the wedge that favour the recycling and exhumation of the subducted material;

(2) during the post-collisional phase, the system warms because of the thermal re-equilibration, producing the dehydration of the wedge and the consequent deactivation of the small convective cells. In addition, a huge amount of the subducted material rises, causing the doubling of the crust over long periods;

(3) the dynamics of the hydrated area is strictly correlated with the thermal state at the external edges of the mantle wedge. When shear heating is not accounted, higher subduction velocities correspond to larger hydrated areas during the early stage of the active oceanic subduction, when the thermal state is controlled by the temperature in the slab. Instead, smaller hydrated areas correlate to higher subduction velocities during the mature stages of the active oceanic subduction, when the thermal state is mainly controlled by the mantle flow;

(4) the occurrence of shear heating decreases the extension of the hydrated area as well as its duration after the collision because of the warming of the mantle wedge;

(5) when both mantle hydration and shear heating are considered the extension of the hydrated area depends by the thermal state in the slab only and higher subduction velocities correspond to larger hydrated areas through the whole active oceanic subduction phase;

(6) during the post-collisional phase, in all models, the hydrated area undergoes an initial widening before an abruptly decrease due to the thermal re-equilibration of the system.

We have also analysed the P–T conditions recorded by exhumed crustal materials and compared them with metamorphic conditions that are traditionally associated to different tectonic settings. Our results show that contrasting P–T conditions can contemporaneously characterize different portions of subduction systems, and conditions that have been traditionally considered to be indicative

of different tectonic environments can be simultaneously recorded. In particular:

(1) Barrovian- (or Dalradian)-type metamorphic conditions also develop during active oceanic subduction before the increase in the T/P ratio associated with the continental collision;

(2) Barrovian P–T conditions are recorded in all models by markers derived from the continental crust of the upper plate and have not deeply involved in the subduction system but simply displaced toward the more internal and shallower portion of the mantle wedge. The P_{maxA} values of these markers were recorded early in their evolution. P–T evolutions compatible with high P/T metamorphic series are recorded by deeply buried markers uplifted in the hydrated wedge;

(3) the slow warming of the system during the early stages of the post-collisional phase promotes P–T conditions that are compatible with the development of Franciscan- (or Sanbagawa)-type metamorphism until 10 Ma after the continental collision;

(4) the subducted markers that reach their P_{maxC} values under Franciscan-type metamorphic conditions during the post-collisional phase are exhumed recording a Barrovian- (or Dalradian)-type metamorphic conditions.

ACKNOWLEDGEMENTS

REFERENCES

Afonso, J.C. & Ranalli, G., 2004. Crustal and mantle strengths in continental lithosphere: is the jelly sandwich model obsolete?, *Tectonophysics,* **394,** 221–232.

Agard, P., Yamato, P., Jolivet, L. & Burov, E., 2009. Exhumation of oceanic blueschists and eclogites in subduction zones: Timing and mechanisms, *Earth-Sci. Rev.,* **92,** 53–79.

Alejano, L.R. & Bobet, A., 2012. Drucker–Prager criterion, rock mechanics and rock engineering, **45**(6), 995–999.

Andrews, D.J. & Sleep, N.H., 1974. Numerical modelling of tectonic flow behind Island Arcs, *Geophys. J. R. astr. Soc.,* **38**(2), 237–251.

Arcay, D., Tric, E. & Doin, M.P., 2005. Numerical simulation of subduction zones. Effect of slab dehydration on the mantle wedge dynamics, *Phys. Earth planet. Inter.,* **149,** 133–153.

Babeyko, A.Y. & Sobolev, S.V., 2008. High-resolution numerical modeling of stress distribution in visco-elasto-plastic subducting slabs, *Lithos,* **103,** 205–216.

Best, M.G. & Christiansen, E.H., 2001. *Igneous Petrology*, pp. 455, Blackwell Science.

Billen, M.I. & Gurnis, M., 2001. A low viscosity wedge in subduction zones, *Earth planet. Sci. Lett.,* **193,** 227–236.

Burov, E. & Yamato, P., 2008. Continental plate collision, P-T–t–z conditions and unstable vs. stable plate dynamics: insights from thermo-mechanical modeling, *Lithos,* **103,** 178–204.

Butler, J.P., Beaumont, C. & Jamieson, R.A., 2014. The Alps 2: controls on crustal subduction and (ultra)high-pressure rock exhumation in Alpine-type orogens, *J. geophys. Res.,* **119,** 5987–6022.

Chopra, P.N. & Peterson, M.S., 1981. The experimental deformation of dunite, *Tectonophysics,* **78,** 453–473.

Christensen, U.R., 1992. An Eulerian Tecnique for thermo-mechanical model of lithospheric extension, *J. geophys. Res.,* **97,** 2015–2036.

Christensen, U.R. & Yuen, D.A., 1985. Layered convection induced by phase transitions, *J. geophys. Res.,* **90**(B12), 10 291–10 300.

Colmenares, L. & Zoback, M., 2002. A statistical evaluation of intact rock failure criteria constrained by polyaxial test data for five different rocks, *Int. J. Rock Mech. Min. Sci.,* **39**(6), 695–729.

Cruciani, C., Carminati, E. & Doglioni, C., 2005. Slab dip vs. lithosphere age: no direct function, *Earth planet. Sci. Lett.,* **238,** 298–310.

Davies, J.H. & Stevenson, D.J., 1992. Physical models of source region of subduction zone volcanics, *J. geophys. Res.,* **97**(B2), 2037–2070.

Dubois, J. & Diament, M., 1997. *Gèophysique*, pp. 201–213, Masson.

Emmanuel, S. & Berkowitz, B., 2006. Suppression and stimulation of seafloor hydrothermal convection by exothermic mineral hydration, *Earth planet. Sci. Lett.,* **243**(3-4), 657–668.

England, P.C. & Thompson, A.B., 1984. Pressure–temperature–time paths of regional metamorphism I. Heat transfer during the evolution of regions of thickened continental crust, *J. Petrol.,* **25**(4), 894–928.

Ernst, W.G. & Liou, J.G., 2008. High- and ultrahigh-pressure metamorphism: past results and future prospects, *Am. Mineral.,* **93,** 1771–1786.

Faccenda, M., 2014. Water in the slab: a trilogy, *Tectonophysics,* **614,** 1–30.

Faccenda, M. & Mancktelow, N.S., 2010. Fluid flow during unbending: implications for slab hydration, intermediate-depth earthquakes and deep fluid subduction, *Tectonophysics,* **494**(1–2), 149–154.

Faccenda, M., Gerya, T.V. & Burlini, L., 2009. Deep slab hydration induced by bending-related variations in tectonic pressure, *Nat. Geosci,* **2**(11), 790–793.

Gerya, T.V., 2010. *Introduction to Numerical Geodynamic Modelling*, pp. 345, Cambridge Univ. Press.   Q6

Gerya, T.V., 2015. Tectonic overpressure and underpressure in lithospheric tectonics and metamorphism, *J. Metamorphic Geol.,* **33,** 785–800.

Gerya, T.V. & Stöckhert, B., 2006. Two-dimensional numerical modeling of tectonic and metamorphic histories at active continental margins, *Int. J. Earth. Sci.,* **95**(2), 250–274.

Gerya, T.V. & Yuen, D.A., 2003. Rayleigh-Taylor instabilities from hydration and melting propel 'cold plumes' at subdaction zones, *Earth planet. Sci. Lett.,* **212,** 47–62.

Gerya, T.V., Stöckhert, B. & Perchuk, A.L., 2002. Exhumation of high-pressure metamorphic rocks in a subduction channel: a numerical simulation, *Tectonics,* **21**(6), 1–15.

Gerya, T.V., Perchuk, L.L. & Burg, J.P., 2008. Transient hot channels: perpetrating and regurgitating ultrahigh-pressure, high-temperature crust–mantle associations in collision belts, *Lithos,* **103,** 236–256.

Gorczyk, W., Gerya, T.V., Connolly, J.A.D., Yuen, D.A. & Rudolph, M., 2006. Large-scale rigid-body rotation in the mantle wedge and its implications for seismic tomography, *Geochem. Geophys. Geosyst.,* **7**(5), 1–23.

Gorczyk, W., Gerya, T.V., Connolly, J.A.D. & Yuen, D.A., 2007a. Growth and mixing dynamics of the mantle wedge plumes, *Geology,* **35,** 587–590.

Gorczyk, W., Guillot, S., Gerya, T.V. & Hattori, K., 2007b. Asthenospheric upwelling, oceanic slab retreat, and exhumation of UHP mantle rocks: insights from Greater Antilles, *Geophys. Res. Lett.,* **34,** L21309.   Q7

Guillot, S., Hattori, K., Agard, P., Schwartz, S. & Vidal, O., 2009. Exhumation processes in oceanic and continental subduction contexts: a review, in *Subduction Zone Dynamics*, pp. 175–204, eds Lallemand,, S., Funiciello & F.Springer-Verlag.

Haenel, R., Rybach, L. & Stegena, L., 1988. *Handbook of Terrestrial Heat-flow Density Determination*, pp. 486, Kluwer Academic Publisher.

Hartz, E.H. & Podladchikov, Y.Y., 2008. Toasting the jelly sandwich: the effect of shear heating on lithospheric geotherms and strength, *Geology,* **36**(4), 331–334.

Hebert, L.B., Antoshechkina, P., Asimow, P. & Gurnis, M., 2009. Emergence of a low-viscosity channel in subduction zones through the coupling of mantle flow and thermodynamics, *Earth planet. Sci. Lett.,* **278**(3–4), 243–256.

Hirth, G. & Guillot, S., 2013. Rheology and tectonic significance of serpentinite, *Elements,* **9**(2), 107–113.

Hirth, G. & Kohlstedt, D.L., 2003. Rheology of the upper mantle and the mantle wedge: a view from the experimentalists, in *Inside the Subduction Factory*, vol. 138, pp. 83–105, ed. Eiler & J.Monograph American Geophys. Union.

Honda, S. & Saito, M., 2003. Small-scale convection under the back-arc occurring in the low viscosity wedge, *Earth planet. Sci. Lett.,* **216,** 703–715.

Ida, Y., 1983. Convection in the mantle wedge above the slab and tectonic processes in subduction zones, *J. geophys. Res.,* **88**(B9), 7449–7456.

Iwamori, H., 1998. Transportation of H_2O and melting in subduction zones, *Earth planet. Sci. Lett.,* **160,** 65–80.

Kirby, S.H., 1983. Rheology of the lithosphere, *Rev. Geophys.,* **21**(6), 1459–1487.

Kornprobst, J., 2002. Metamorphic rocks and their geodynamic significance, in *A Petrological Handbook,* vol. 12, pp. 206, Petrology and Structural Geology Series, Kluwer.

Lallemand, S., Heuret, A. & Boutelier, D., 2005. On the relationships between slab dip, back-arc stress, upper plate absolute motion, and crustal nature in subduction zones, *Geochem. Geophys. Geosyst.,* **6,** Q09006.

Le Voci, G., Davies, D.R., Goes, S., Kramer, S.C. & Wilson, C.R., 2014. A systematic 2-D investigation into the mantle wedge's transient flow regime and thermal structure: complexities arising from a hydrated rheology and thermal buoyancy, *Geochem. Geophys. Geosyst.,* **15**(1), 28–51.

Liu, L., Zhang, J., Green, H.W., Jin, Z. & Bozhilov, K.N., 2007. Evidence of former stishovite in metamorphosed sediments, implying subduction to >350 km, *Earth planet. Sci. Lett.,* **263,** 180–191.

Maierová, P., Schulmann, K., Lexa, O., Guillot, S., Štípská, P., Janoušek, V. & Čadek, O., 2016. European Variscan orogenic evolution as an analogue of Tibetan–Himalayan orogen: insights from petrology and numerical modeling, *Tectonics,* **35,** 1–21.

Marotta, A.M. & Spalla, M.I., 2007. Permian-Triassic high thermal regime in the Alps: Result of late Variscan collapse or continental rifting? Validation by numerical modeling, *Tectonics,* **26,** 1–27.

Marotta, A.M., Spelta, E. & Rizzetto, C., 2006. Gravity signature of crustal subduction inferred from numerical modelling, *Geophys. J. Int.,* **166,** 923–938.

Marotta, A.M., Roda, M., Conte, K. & Spalla, M.I., 2016. Thermomechanical numerical model of the transition from continental rifting to oceanic spreading: the case study of the Alpine Tethys, *Geol. Mag.,* 1–30.

Minakov, A., Podladchikov, Y., Faleide, J. & Huismans, R., 2013. Rifting assisted by shear heating and formation of the Lomonosov Ridge, *Earth planet. Sci. Lett.,* **373,** 31–40.

Miyashiro, A., 1961. Evolution of Metamorphic Belts, *J. Petrol.,* **2**(3), 277–311.

Miyashiro, A., 1973. Paired and unpaired metamorphic belts, *Tectonophysics,* **17**(3), 241–254.

Nagaya, T., Walker, A.M., Wookey, J., Wallis, S.R., Ishii, K. & Kendall, J.M., 2016. Seismic evidence for flow in the hydrated mantle wedge of the Ryukyu subduction zone, *Sci. Rep.,* **6,** 29981.

Nicollet, C., 2010. *Métamorphisme et géodynamique*, pp. 288, *Dunod*.

Peacock, S.M., 1996. Thermal and petrologic structure of subduction zones, in *Subduction: Top to Bottom*, Geophysical Monograph Series, vol. 96, pp. 119–133, ed. Bebout,, G.E.

Pérez-Gussinyé, M. & Reston, T.J., 2001. Rheological evolution during extension at nonvolcanic rifted margins: onset of serpentinization and development of detachments leading to continental breakup, *J. geophys. Res.,* **106**(B3), 3961–3975.

Polino, R., Dal Piaz, G.V. & Gosso, G., 1990. Tectonic erosion at the Adria margin and accretionary processes for the Cretaceous orogeny of the Alps., *Mem. Soc. Geol. France,* **156,** 345–367.

Quinquis, M.E.T. & Buiter, S.J.H., 2014. Testing the effects of basic numerical implementations of water migration on models of subduction dynamics, *Solid Earth,* **5**(1), 537–555.

Ranalli, G. & Murphy, D.C., 1987. Rheological stratification of the lithosphere, *Tectonophysics,* **132**(4), 281–295.

Roda, M., Marotta, A.M. & Spalla, M.I., 2010. Numerical simulations of an ocean–continent convergent system: Influence of subduction geometry and mantle wedge hydration on crustal recycling, *Geochem. Geophys. Geosyst.,* **11**(5).

Roda, M., Marotta, A.M. & Spalla, M.I., 2011. The effects of the overriding plate thermal state on the slab dip in an ocean–continent subduction system, *C. R. Acad. Sci., Paris,* **343,** 323–330.

Roda, M., Spalla, M.I. & Marotta, A.M., 2012. Integration of natural data within a numerical model of ablative subduction: a possible interpretation for the Alpine dynamics of the Austroalpine crust, *J. Metamorphic Geol.,* **30**(9), 973–996.

Rosas, J.C., Currie, C.A., Harris, R.N. & He, J., 2016. Effect of hydrothermal circulation on slab dehydration for the subduction zones of Costa Rica and Nicaragua, *Phys. Earth planet. Inter.,* **255,** 66–79.

Rüpke, L.H., Morgan, J.P., Hort, M. & Connolly, J.A., 2004. Serpentine and the subduction zone water cycle, *Earth planet. Sci. Lett.,* **223**(1–2), 17–34.

Rüpke, L.H., Schmid, D.W., Perez-Gussinye, M. & Hartz, E., 2013. Interrelation between rifting, faulting, sedimentation, and mantle serpentinization during continental margin formation—including examples from the Norwegian Sea, *Geochem. Geophys. Geosyst.,* **14**(10), 4351–4369.

Schmidt, M.W. & Poli, S., 1998. Experimentally based water budgets for dehydrating slabs and consequences for arc magma generation, *Earth planet. Sci. Lett.,* **163,** 361–379.

Souche, A., Medvedev, S., Andersen, T.B. & Dabrowski, M., 2013. Shear heating in extensional detachments: implications for the thermal history of the Devonian basins of W Norway, *Tectonophysics,* **608,** 1073–1085.

Spalla, M.I., Lardeaux, J.M., Dal Piaz, G.V., Gosso, G. & Messiga, B., 1996. Tectonic significance of the Alpine eclogites, *J. Geodyn.,* **21**(3), 257–285.

Spear, F.S., 1993. *Metamorphic Phase Equilibria and Pressure-Temperature-Time Paths*, pp. 789, Min. Soc. Am. Monograph.

Stern, R.J., 1998. A subduction primer for instructors of introductory geology courses and authors of introductory geology textbooks, *J. Geosci. Educ.,* **46,** 221–228.

Stöckhert, B. & Gerya, T.V., 2005. Pre-collisional high pressure metamorphism and nappe tectonics at active continental margins: a numerical simulation, *Terra Nova,* **17,** 102–110.

Tao, W.C. & O'Connell, R.J., 1992. Ablative subduction: A two-sided alternative to the conventional subduction model, *J. geophys. Res.,* **97**(B6), 8877–8904.

Thielmann, M. & Kaus, B.J., 2012. Shear heating induced lithospheric-scale localization: Does it result in subduction?, *Earth planet. Sci. Lett.,* **359–360,** 1–13.

Thompson, A.B., 1981. The pressure – temperature (P,T) plane viewed by geophysicists and petrologists, *Terra Cognita,* **1,** 11–20.

Thompson, A.B. & England, P.C., 1984. Pressure–temperature–time paths of regional metamorphism II. Their inference and interpretation using mineral assemblages in metamorphic rocks, *J. Petrol.,* **25**(4), 929–955.

Turcotte, D.L. & Schubert, G., 2002. *Geodynamics,* 2nd edn, Cambridge Univ. Press.

Uyeda, S. & Kanamori, H., 1979. Back-arc opening and the model of subduction, *J. geophys. Res.,* **84**(8), 1049–1061.

Von Raumer, J.F., Stampfli, G.M. & Bussy, F., 2003. Gondwana-derived microcontinents—the constituents of the Variscan and Alpine collisional orogens, *Tectonophysics,* **365,** 7–22.

Wilson, C.R., Spiegelman, M., van Keken, P.E. & Hacker, B.R., 2014. Fluid flow in subduction zones: the role of solid rheology and compaction pressure, *Earth planet. Sci. Lett.,* **401,** 261–274.

Yamato, P., Agard, P., Burov, E., Pourhiet, L.L., Jolivet, L. & Tiberi, C., 2007. Burial and exhumation in a subduction wedge: Mutual constraints from thermomechanical modeling and natural P-T-t data (Schistes Lustrés, western Alps), *J. geophys. Res.,* **112,** 1–28.

20   *A. Regorda* et al.

APPENDIX A: DETAILS OF THE MODEL FORMULATIONS

A1 Rheology

Outside the lithosphere, the effective viscosity is calculated as follows:

$$\mu^{\text{eff}} = \mu_{\text{viscous}} = \mu_{0,\text{m}}\, e^{\left[\frac{E_i}{R}\left(\frac{1}{T} - \frac{1}{T_0}\right)\right]} \tag{A1}$$

where $\mu_{0,m}$ and E_m are the reference viscosity at the reference temperature T_0 and the activation energy for the mantle, respectively.

We combine the viscous rheology with a brittle/plastic rheology within the lithospheric layer, thereby defining the effective viscosity as follows:

$$\mu^{\text{eff}} = \min\left\{\mu_{\text{viscous}}, \mu_{\text{plastic}}\right\} \tag{A2}$$

Different yield criteria are used in the geoscience field to define the plastic yield of rocks, such as the Drucker–Prager, the von-Mises–Hencky and the Tresca criteria.

The Drucker–Prager criterion states that yielding depends on both the second invariant of the stress deviator and the first invariant of the stress tensor. Although the Drucker–Prager criterion is simple and predicts a smooth and symmetric failure surface, which facilitates its implementation in numerical models, a major limitation of this criterion is that it overestimates the rock strength and predicts errors that are larger than other yield criteria (Colmenares & Zoback 2002; Alejano & Bobet 2012). The Drucker–Prager criterion can be considered as an extension of the von-Mises–Hencky criterion and states that yielding occurs when the second invariant of the stress, which is defined by the magnitude of either the maximum and intermediate principal stress components, reaches a value that is characteristic of the material (e.g. Ranalli & Murphy 1987).

The von-Mises–Hencky criterion is similar to the Tresca criterion, although the latter states that yielding depends on the magnitude of only the maximum principal stress. Because the Tresca criterion is a more conservative plastic yielding criterion, we use it to determine the plastic viscosity.

The Tresca criterion requires that the principal stress difference as well as the principal stresses themselves to be less than the yield stress σ_Y (Turcotte & Schubert 2002):

$$|\sigma_1| \leq \sigma_Y; \quad |\sigma_2| \leq \sigma_Y; \quad |\sigma_1 - \sigma_2| \leq \sigma_Y. \tag{A3}$$

After performing minor mathematical steps, we can define the plastic viscosity as follows:

$$\mu_{\text{plastic}} = \min\{\mu_1, \mu_2, \mu_3\} \tag{A4}$$
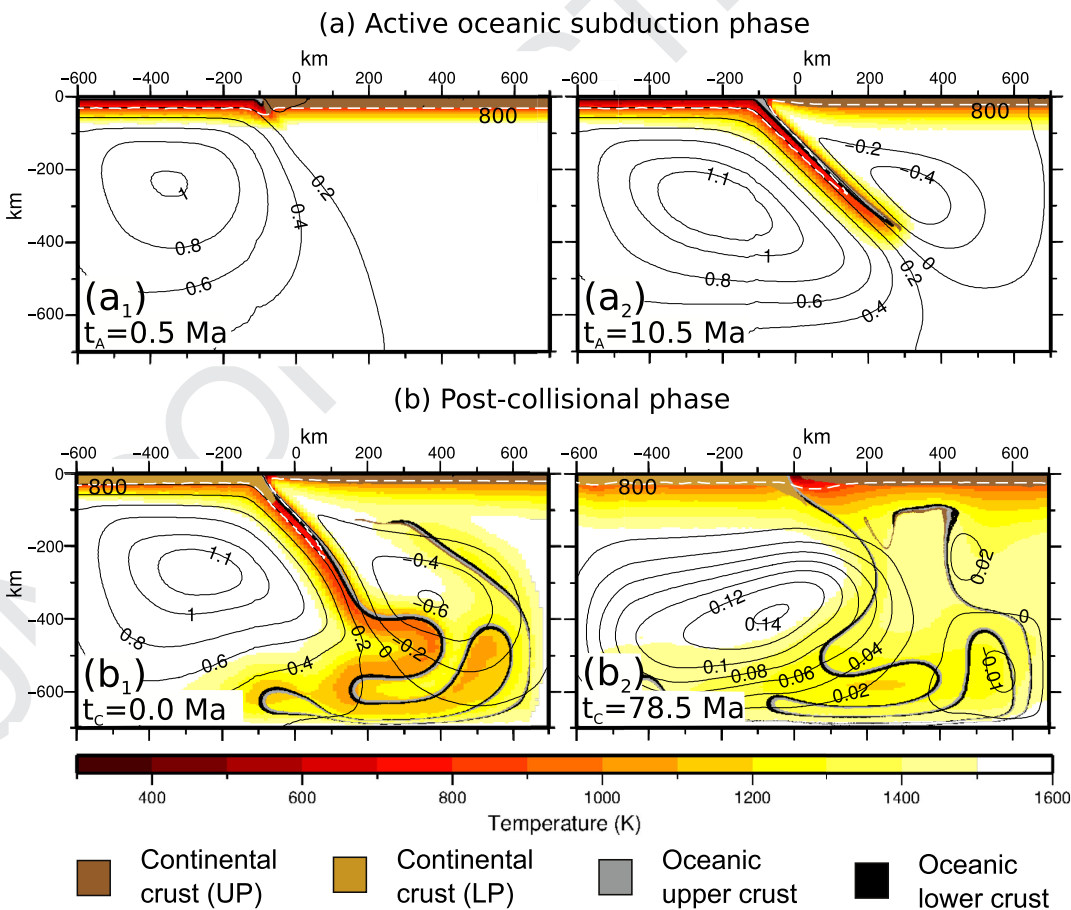

Figure A1. Large-scale temperature field (colours) and streamline patterns (solid black lines) predicted by model REF.5 at different times during the active oceanic subduction phase (a) and the post-collisional phase (b). t_A indicates times from the beginning of the active oceanic subduction phase; t_C indicates times from the beginning of the post-collisional phase. The dashed white lines indicate the 800 K isotherm. Numbers on streamlines are indexes of the intensity of the flow. UP stands for upper plate; LP stands for lower plate.
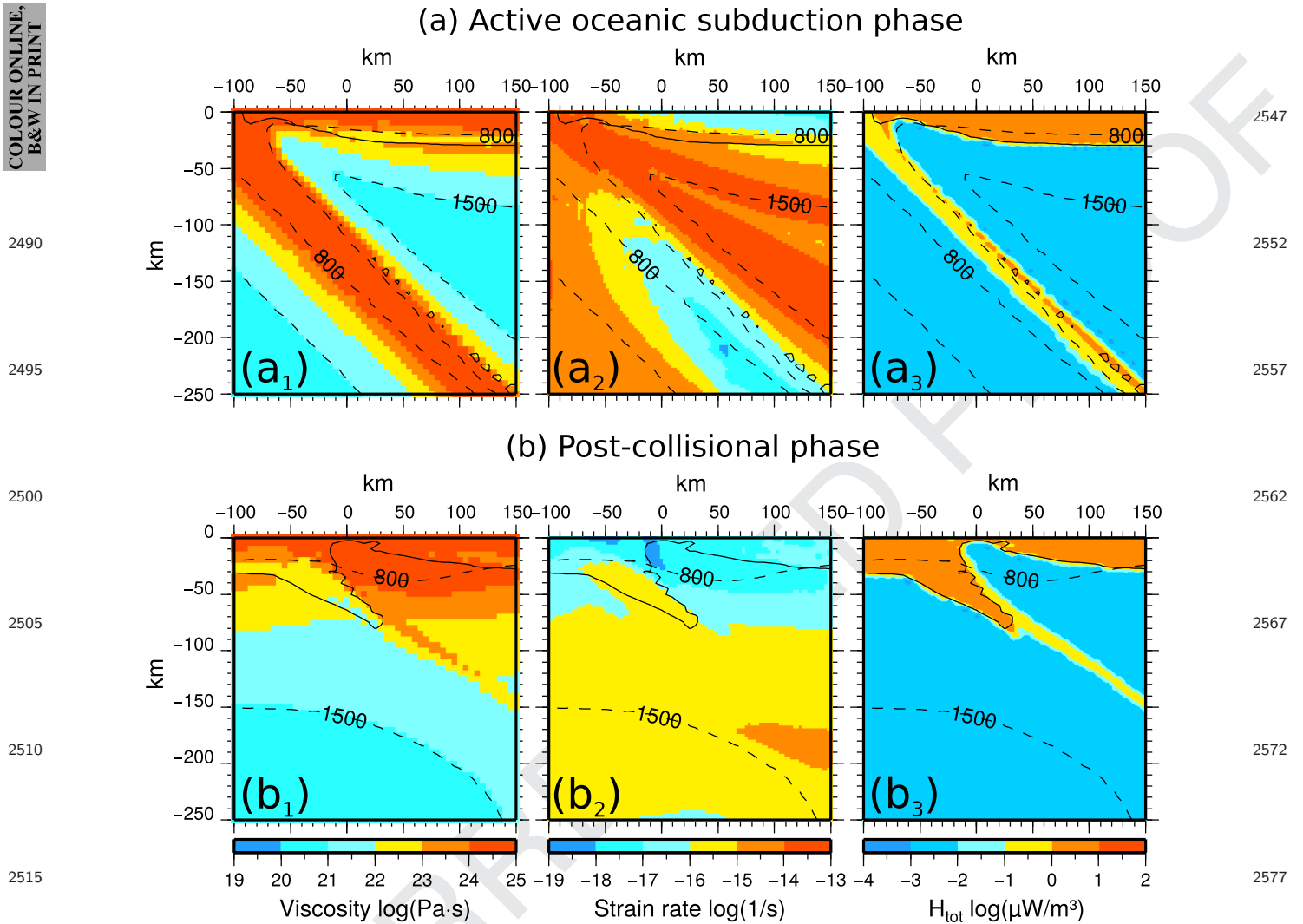
(a) Active oceanic subduction phase

(b) Post-collisional phase

Figure A2. Distribution of the effective viscosity (a_1 and b_1), strain rate (a_2 and b_2) and total energy (a_3 and b_3) predicted by model REF.5 at 10.5 Ma after the beginning of active oceanic subduction phase (a) and at the end of the post-collisional phase (b). The dashed black lines indicate the 800 and 1500 K isotherms. The solid black lines indicate the base of the continental crust.

with

$$\mu_1 = \frac{\sigma_Y - P}{2\dot{\epsilon}_1}; \quad \mu_2 = \frac{\sigma_Y - P}{2\dot{\epsilon}_2}; \quad \mu_3 = \frac{\sigma_Y}{2(\dot{\epsilon}_1 - \dot{\epsilon}_2)} \qquad (A5)$$

where P is the pressure, and $\dot{\epsilon}_i$ represent the principal strain rates.

The yield stress σ_Y is defined by assuming the following simplified formulation of Byerlee's law criterion:

$$\sigma_Y = \beta \cdot y \quad \text{with} \quad \beta = 40\,\text{MPa km}^{-1} \qquad (A6)$$

where the effects of pore fluid pressure are neglected and ρ and y are the density and the depth, respectively.

A2 Hydration and serpentinization within the wedge area

We simulate the maximum dehydration depth of the oceanic crust, Y_{dehydr}, below which the water content in hydrous phases in H_2O-saturated MORB basalt is negligible, using the stability field of lawsonite (Roda *et al.* 2010 and references therein) as follows:

$$Y_{\text{dehydr}} = -0.8755 \cdot T_{\text{imarc}} + 714.35 \qquad (A7)$$

where Y_{dehydr} is calculated for each oceanic crustal marker with temperature T_{imarc} up to a depth of 300 km. Although Schmidt & Poli (1998) indicate that the slab is mostly dehydrated at a depth of 150–200 km, exhumation of subducted continental rocks with stishovite suggests that water can be transported up to depths of 250–300 km (Liu *et al.* 2007). Furthermore, Faccenda *et al.* (2009), Faccenda & Mancktelow (2010) and Faccenda (2014) have shown that tectonic stresses can influence the hydration pattern in the subducted slab, thereby allowing fluids to penetrate in the slab and favouring their transport to great depths up to the base of the upper mantle. The presence of hydrothermal circulation in the oceanic crust can affect the thermal state in the subducting slab, which generates higher hydrous phase stability at higher depths compared with those predicted by classical thermal models of the subduction zone (Perry *et al.* 2016; Rosas *et al.* 2016). However, the hydrothermal circulation does not have a significant impact on the depth of dehydration reactions at shallow depths (Rosas *et al.* 2016).

Because the lithostatic pressure is much greater than the dynamic pressure (Babeyko & Sobolev 2008; Burov & Yamato 2008; Butler *et al.* 2014; Gerya 2015), it has been neglected; thus, the depth scaled
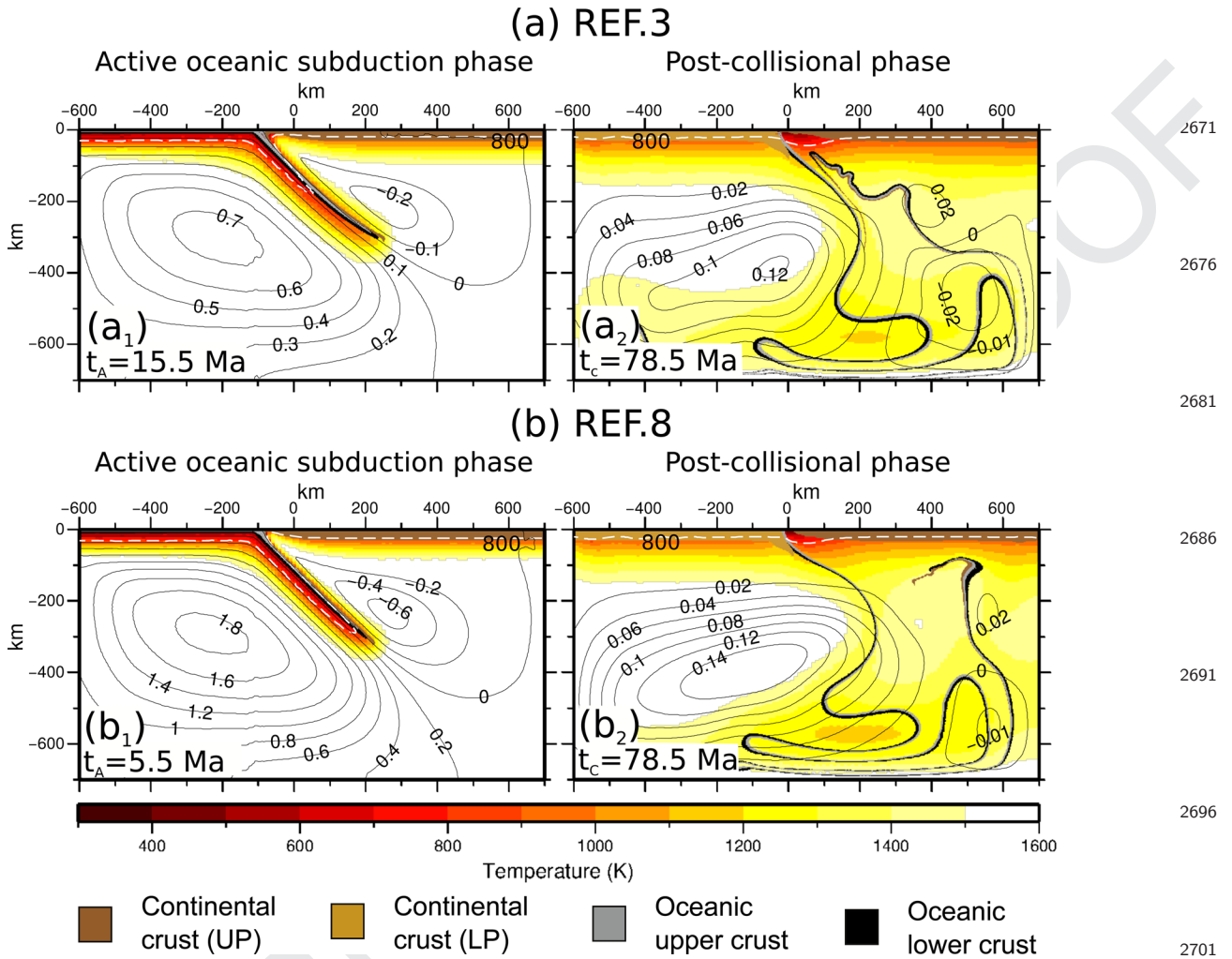
Figure A3. Large-scale temperature field (colours) and streamline patterns (solid black lines) predicted by models REF.3 (a) and REF.8 (b) at different times during the active oceanic subduction phase (panels a_1 and b_1) and the post-collisional phase (panels a_2 and b_2). t_A indicates times from the beginning of the active oceanic subduction phase; t_C indicates times from the beginning of the post-collisional phase. The dashed white lines indicate the 800 K isotherm. Numbers on streamlines are indexes of the intensity of the flow. Different ages have been chosen in order to compare similar evolutionary stages of oceanic subduction for different velocities, such as similar depths reached by slab. UP stands for upper plate; LP stands for lower plate.

by the density is used here to define the progressive hydration of the mantle wedge. Then, the stability field of serpentine is calculated for each element by using the following two equations (Roda *et al.* 2010 and references therein):

$$Y_{hydr} = -0.3394 \cdot T_{elem} + 268.09 \quad \text{above 66 km depth}$$
$$Y_{hydr} = 0.954 \cdot T_{elem} + 993.28 \quad \text{below 66 km depth} \tag{A8}$$

where Y_{hydr} represents the maximum hydration depth and T_{elem} is the elemental temperature. Each element with an average depth and temperature (Y_{elem}, T_{elem}) is considered to be hydrated if $Y_{hydr} < Y_{elem} < Y_{dehydr}$, where Y_{hydr} is calculated from A_{11}. The subducting plate limits the hydrated area from below. Specifically, to better delineate the geometry of the lower border of the hydrated area, the subducted plate is subdivided into segments of equal length, and the deepest dehydrated oceanic crust marker for each segment is identified at each time during the system's dynamic evolution. The line that connects these markers defines the lower limit of the hydrated area.

A3 Crust–mantle differentiation

To differentiate the crust from the mantle, we use the Lagrangian particle technique (e.g. Christensen 1992) as implemented in Marotta & Spalla (2007) and Roda *et al.* (2010). At the beginning of the evolution, 288 061 markers identified by different indexes are spatially distributed (Fig. 1) at a density of 1 marker per 0.25 km^2 to define the upper oceanic crust, the lower oceanic crust and the continental crust.

During the evolution of the system, each particle (marker) is advected using a first-order (both in time and in space) Runge–Kutta scheme. At each time, the elemental density of each type of particle defines the composition of each element of the grid, C^e, such as $C^e = C^e_{oc_U} + C^e_{oc_L} + C^e_{cc}$, where $C^e_{oc_U} = N^e_{oc_U}/N^e_0$, $C^e_{oc_L} = N^e_{oc_L}/N^e_0$ and $C^e_{cc} = N^e_{cc}/N^e_0$ are the elemental densities of the upper oceanic crust-type, lower oceanic crust-type and continental crust-type particles, respectively, $N^e_{oc_U}$, $N^e_{oc_L}$ and N^e_{cc} are the numbers of the upper oceanic crust-type, lower oceanic crust-type and continental crust-type particles within element e, respectively, and N^e_0 is the maximum number of particles of any type that the element e can contain.
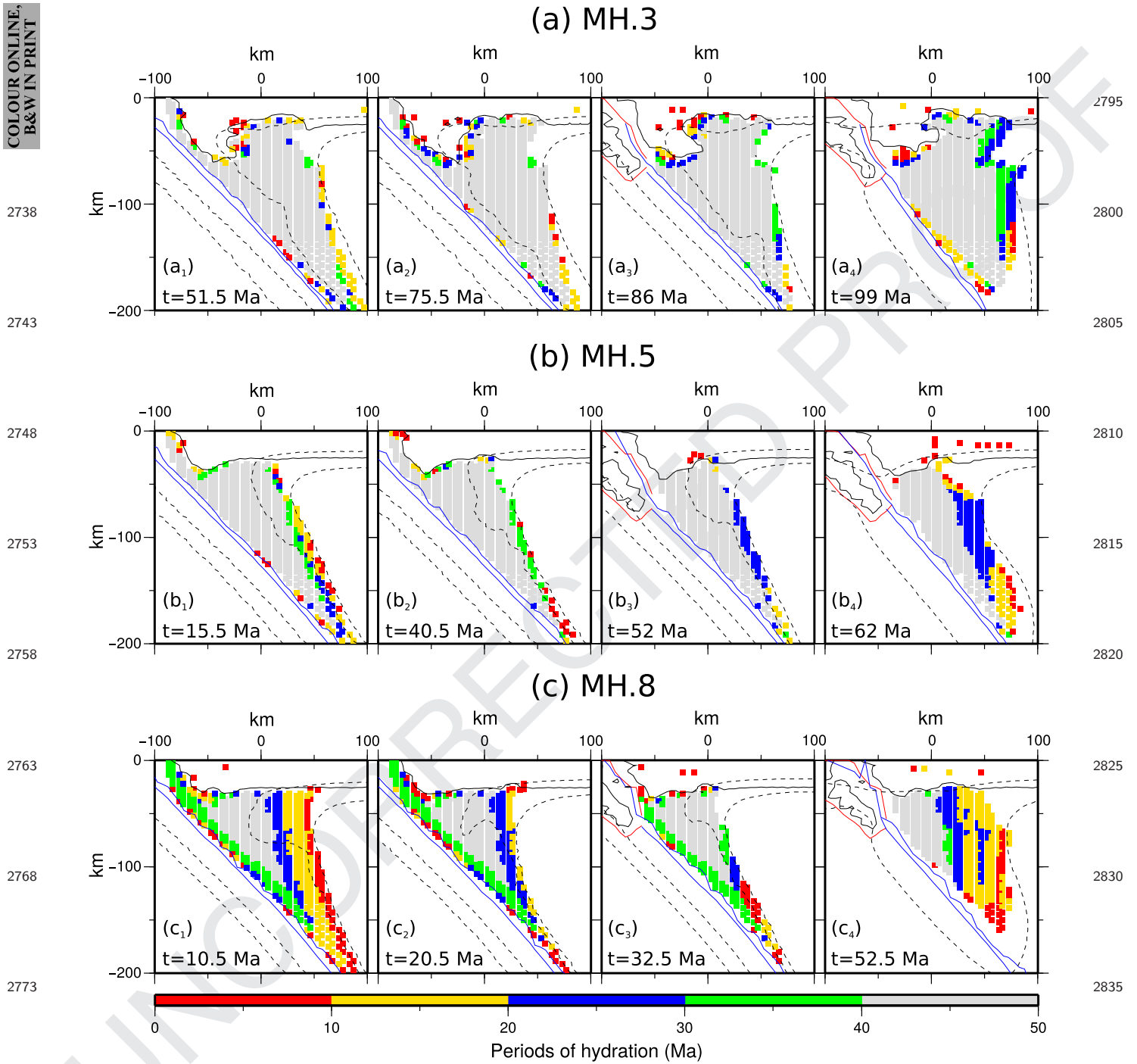
Figure A4. Spatial configurations of the hydrated area at different times of evolution from the beginning of the active oceanic subduction phase for MH.3 (a), MH.5 (b) and MH.8 (c) models. The elements are coloured according to their periods of hydration. The elements with hydration that lasted longer than 40 Ma (grey squares) constitute the main hydrated area. The dashed black lines indicate the 800 K and 1000 K isotherms. The black, red and blue solid lines identify the upper continental crust, the lower continental crust and the upper oceanic crust, respectively.

All of the properties (conductivity, specific heat at a constant pressure, density and viscosity) depend on the composition such that within each element e, the value of property P^e can be expressed as follows

$$P^e = \mathrm{P}_m \left[1 - \sum_i C_i^e \right] + \sum_i P_i C_i^e \qquad \text{(A9)}$$

where P_m is the value of the property for the mantle, and P_i is the value of the property for the serpentinized mantle ($i = \mathrm{sm}$), upper oceanic crust ($i = \mathrm{oc}_U$), lower oceanic crust ($i = \mathrm{oc}_L$) and continental crust ($i = \mathrm{cc}$).

The density and viscosity also depend on temperature. The density is expressed as follows:

$$\rho^e \left(C^e, \mathrm{T} \right) = \rho_0 \left[1 - \alpha \left(T - T_0 \right) \right] - \sum_i \Delta \rho_i^e C_i^e \qquad \text{(A10)}$$
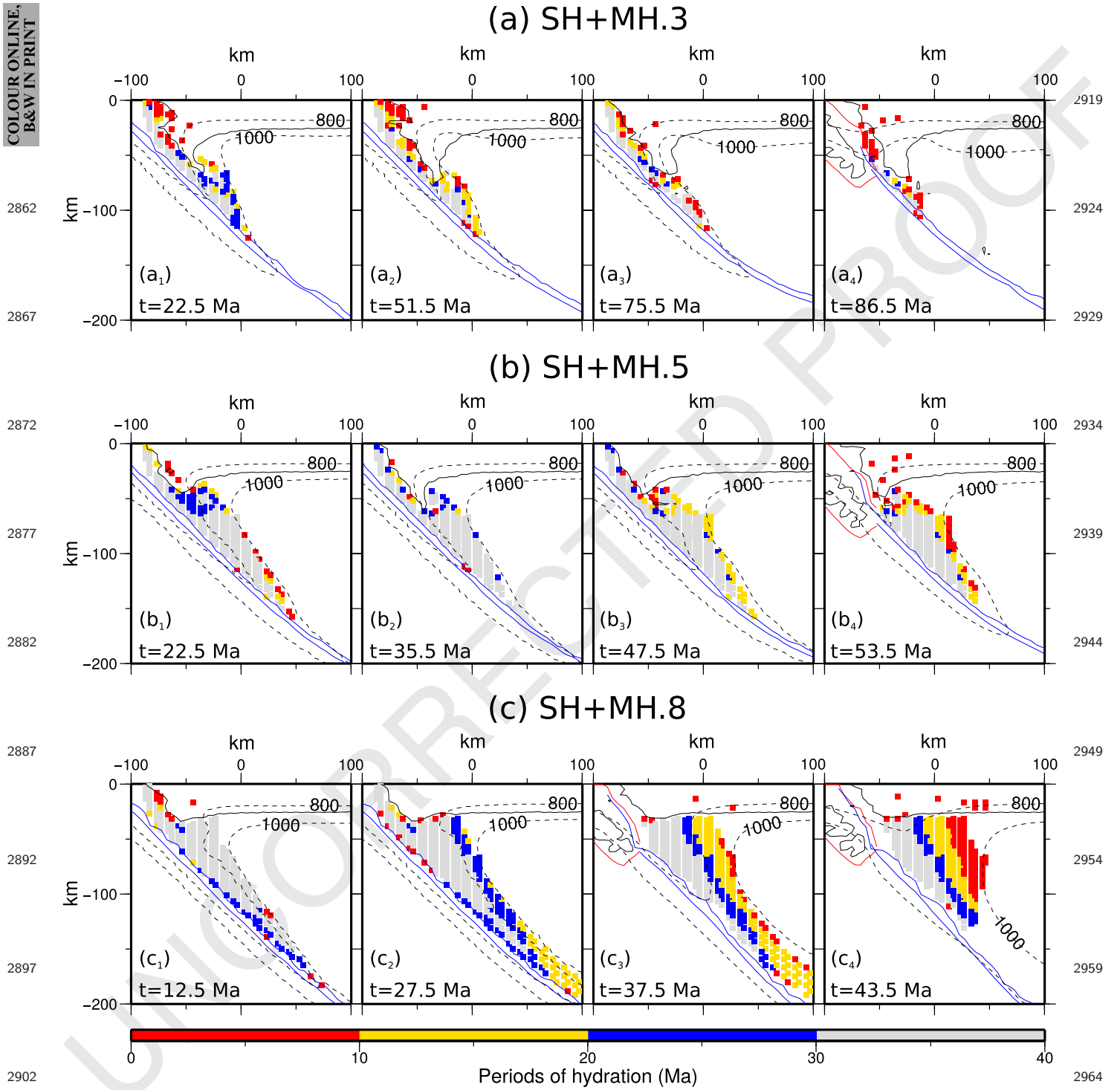
Figure A5. Spatial configurations of the hydrated area at different times of evolution from the beginning of the oceanic subduction for SH+MH.3 (a), SH+MH.5 (b) and SH+MH.8 (c) models. The elements are coloured according to their periods of hydration. The elements with hydration that lasted longer than 30 Ma (grey squares) constitute the main hydrated area. The dashed black lines indicate the 800 K and 1000 K isotherms. The black, red and blue solid lines identify the upper continental crust, the lower continental crust and the upper oceanic crust, respectively.

where the index i identifies the particle type as specified above, α is the thermal coefficient of the volumetric thermal expansion, ρ_0 is the reference density of the mantle at the reference temperature T_0, and $\Delta\rho_i^e$ represent the differences between ρ_0 and the density of the upper oceanic crust, $\Delta\rho_{oc_U}^e = (\rho_{oc_U} - \rho_0)$, lower oceanic crust, $\Delta\rho_{oc_L}^e = (\rho_{oc_L} - \rho_0)$, and continental crust, $\Delta\rho_{cc}^e = (\rho_{cc} - \rho_0)$.

The viscosity varies within each element according to

$$\mu^e\left(C^e, \mathrm{T}\right) = \mu_m \left[1 - \sum_i C_i^e\right] + \sum_i \mu_i C_i^e \qquad (A11)$$

and

$$\mu_i = \mu_{0,i}\, e^{\left[\frac{E_i}{R}\left(\frac{1}{T} - \frac{1}{T_0}\right)\right]} \qquad (A12)$$

where $\mu_{0,i}$ is the reference viscosity at the reference temperature T_0, and E_i and n_i are the activation energy and exponent, respectively, of the power law for the mantle, upper oceanic crust, lower oceanic crust and continental crust.

APPENDIX B: THERMOMECHANICS OF THE REFERENCE MODEL (REF)

During active oceanic subduction, a convective mantle flow develops underneath the continental overriding plate, which is driven by the progressive descent of the subducting plate, and the convective cells progressively enlarge toward the bottom of the domain (Fig. A1a). Within the first 10 Ma, the mantle flow induces the thermomechanical erosion of the upper plate up to 150 km from the trench (Fig. A1a$_2$) and increases the temperature of the inner portion of the supra-subductive mantle wedge. After 10 Ma, the temperature in the mantle wedge remains stable. The viscosity inside the cold subducting lithosphere is three to four orders of magnitudes higher than that in the mantle wedge area (Fig. A2a$_1$). The strain rates vary from 10^{-16} s^{-1} inside the lower and the upper plates to 10^{-13} s^{-1} in the mantle wedge area (Fig. A2a$_2$). The total energy of the system depends only on the radiogenic heat, which is up to three orders of magnitude higher in the continental crust than the mantle wedge (Fig. A2a$_3$).

An increase in the prescribed subduction velocity enhances the intensity of the mantle flow underneath the overriding plate (Figs A3a$_1$ and b$_1$), which raises the temperature of the mantle wedge (see the isotherm 800 K in Figs A3a$_1$ and b$_1$), as suggested by previous models (e.g. Andrews & Sleep 1974; Uyeda & Kanamori 1979; Davies & Stevenson 1992; Peacock 1996; Stern 1998). However, the subducted lithosphere is colder for higher velocities of subduction. As the slabs heats up by conduction, cold sections of the slab reach greater depths than if they were moving with a slower velocity (see the isotherm 800 K in Figs A3a$_1$ and b$_1$).

The velocity field during the post-collisional phase is comparable in all REF models regardless of the prescribed subduction velocity because the system is driven by gravitational forces only (Figs A1b$_2$, A3a$_2$ and b$_2$). Both the intensity of the velocity field in the mantle wedge area and the large-scale convective flow underneath the lower plate decrease by up to one order of magnitude with respect to those of the active oceanic subduction phase (Fig. A1b$_2$). The large-scale convective flow gradually expands laterally towards the overriding plate, reducing the slab dip (Fig. A1b$_2$). The convective flow underneath the upper continental plate disappears, which induces a thermal re-equilibration in the entire system, with a warming of the subducted lithosphere and a cooling of the mantle wedge (Fig. A1b$_2$). Consequently, the viscosity decreases in the subducted lithosphere and increases in the wedge area, both up to three orders of magnitude (Fig. A2b$_1$). The strain rate decreases throughout the entire domain, by at least three orders of magnitude (Fig. A2b$_2$).

APPENDIX C: DETAILS OF THE EVOLUTION OF THE HYDRATED AREA

C1 MH models

The hydration starts within 1 Ma after the beginning of the active oceanic subduction phase (continuous lines in Fig. 8a) and continues over a period that decreases with the increasing prescribed velocity. In particular the hydration lasts approximately 128 Ma (MH.3),

85 Ma (MH.5) and 66 Ma (MH.8; red, green and blue lines in Fig. 8a, respectively). The velocity of subduction also influences the growth rate, the maximum extension and the variation in time of the dimension of the hydrated areas, because of the strong relation between velocity and thermal fields. In particular, during the early stages of the active oceanic subduction, slower velocities correspond to both lower growth rate and smaller hydrated areas. In fact, after 10 Ma of oceanic subduction the hydrated area has an extension of approximately 6700 km^2 (MH.3), 8750 km^2 (MH.5) and 12 000 km^2 (MH.8). During the advanced stages of active oceanic subduction, the predicted thermal field in the wedge area is mainly controlled by the mantle flow, which is more intense in model MH.8 than in model MH.3. As consequence, model MH.3 undergoes a continuous cooling throughout the active oceanic subduction phase, which produces a gradual increase in the extension of the hydrated area (red line in Fig. 8a) until a maximum of approximately 12 000 km^2, reached after 48 Ma (P$_{3.1}$ in Fig. 8a). Successively, the hydrated area decreases of approximately 1000 km^2 before a new increase up to a new maximum of about 12 000 km^2 at 75 Ma (P$_{3.2}$ in Fig. 8a). Models MH.5 and MH.8 are characterized by an initial cooling phase and a successive rapid warming, which produces a significant decrease in the extension of the hydrated area (green and blue lines in Fig. 8a, respectively). In particular, in model MH.5 the hydrated area reaches a maximum of approximately 9500 km^2 after 15 Ma (P$_{5.1}$ in Fig. 8a), while in model MH.8 the maximum extension is of about 12 000 km^2, after 10 Ma (P$_{8.1}$ in Fig. 8a).

In all MH models the main hydrated area persists for a minimum of 40 Ma. The dimension of the main hydrated area increases with decreasing velocity during the active oceanic subduction phase. The main hydrated area has a maximum extension of approximately 9500 km^2 (MH.3), 6750 km^2 (MH.5) and 3100 km^2 (MH.8; red, green and blue lines in Fig. 8a, respectively). The main hydrated areas (grey areas in Fig. A4) extend up to a depth of 200 km (MH.3, Fig. A4a), 180 km (MH.5, Fig. A4b) and 120 km (MH.8, Fig. A4c).

The secondary smaller hydrated areas are mostly located along the external and deepest portions of the main hydrated area, increasing the total extension of the hydrated area after the collision by several hundreds of square kilometres. Two main episodes of growth of secondary hydrated areas occur for model MH.3, while only one episode occurs for models MH.5 and MH.8. In particular, in model MH.3 the first episode of growth occurs at approximately 50 Ma and is associated to secondary areas that remain hydrated for periods between 1 and 20 Ma (red and yellow squares in Fig. A4a$_1$), while the second episode occurs at approximately 75 Ma, related to secondary areas that remain hydrated for periods between 1 and 10 Ma (red squares in Fig. A4a$_2$). In model MH.5, the unique episode of growth occurs at approximately 15 Ma and is related to secondary areas that remain hydrated for periods between 10 and 20 Ma (yellow squares in Fig. A4b$_1$), while in model MH.8 the unique episode of growth occurs at approximately 10 Ma and is associated to secondary areas that remain hydrated for periods between 1 and 20 Ma (red and yellow squares in Fig. A4c$_1$).

At the collision, the hydrated area decreases abruptly by approximately 800 km^2 (MH.3), approximately 1400 km^2 (MH.5) and approximately 1000 km^2 (MH.8) (red, green and blue lines in Fig. 8a, respectively). This decrease follows the partial subduction of the continental crust of the lower plate, which confines the low viscosity hydrated channel between the upper plate and the subducting lithosphere. An important change in the boundaries of the hydrated area occurs after the collision when the growth of

secondary hydrated areas results in an increase in the extension of the hydrated area of few thousands of square kilometres. In particular, the growth of the hydrated area after the collision in model MH.3 is related to the growth of secondary areas that remain hydrated for periods between 20 and 40 Ma and it results in an increase of approximately 1000 km^2 (blue and green squares in Fig. A4a$_4$); in model MH.5 it is associated to the growth of secondary areas that remain hydrated for periods between 10 and 30 Ma (yellow and blue squares in Fig. A4b$_4$); finally, in model MH.8 the growth of the hydrated area is related to the growth of secondary areas that remain hydrated for periods between 1 and 30 Ma (red, yellow and blue squares in Fig. A4c$_4$).

C2 SH+MH models

As observed in MH models, the evolution of the hydrated area is strongly affected by the subduction velocity. Hydration starts within 1 Ma from the beginning of the active oceanic subduction phase and it continues over a period that decreases with the increase of the prescribed velocity, lasting 87.8 Ma (SH+MH.3; red line in Fig. 8b), 55.7 Ma (SH+MH.5; green line in Fig. 8b) and 50.3 Ma (SH+MH.8; blue line in Fig. 8b). During the early stages of the active oceanic subduction phase, as for MH models, the mean growth rate of the hydrated area increases with increasing prescribed velocity (dashed lines in Fig. 8b).

During the active oceanic subduction phase, differently from MH models, the maximum extent of both the hydrated areas and the main hydrated areas increase with increasing prescribed velocity, respectively 2500 and 875 km^2 in the SH+MH.3 model (red lines in Fig. 8b), 4250 and 2875 km^2 in the SH+MH.5 model (green lines in Fig. 8b) and 8160 and 3750 km^2 in the SH+MH.8 model (blue lines in Fig. 8b). This is consistent with the lower temperatures in the mantle wedge predicted with intermediate and high convergence velocities. Extension maxima are observed after approximately 24 and 52 Ma for SH+MH.3 (P$_{3.1}$ and P$_{3.2}$ in Fig. 8b) and after approximately 22 and 48 Ma for SH+MH.5 (P$_{5.1}$ and P$_{5.2}$ in Fig. 8b). In model SH+MH.8, however, there is a progressive enlargement of the hydrated area, until a maximum is reached just before the continental collision (P$_{8.1}$ in Fig. 8b).

During the entire active oceanic subduction phase, the main hydrated areas (grey areas in Fig. A5) extend from maximum depths of about 110 km for slow velocities (SH+MH.3; Fig. A5a) and 150 km for moderate and high velocities (SH+MH.5 and SH+MH.8; Figs A5b and c, respectively) to shallow depths, where the areas extend along a narrow 45° dipping channel between the overriding and the subducting plates. The occurrence and locations of the secondary hydrated areas are controlled by the periodic fluctuations in the local thermal state that characterize the margins of the main hydrated area and determine the growth of both the external and deep portions of the total hydrated areas.

Two main episodes of growth of secondary hydrated areas occur for models SH+MH.3 and SH+MH.5 (P$_{3.1}$, P$_{5.1}$, P$_{3.2}$ and P$_{5.2}$ in Fig. 8B, respectively). For model SH+MH.3, the first episode is associated with areas that remain hydrated for less than 10 Ma (red areas in Fig. A5a$_1$) and periods between 20 and 30 Ma (blue colours in Fig. A5a$_1$), while the second episode is associated with secondary areas that remain hydrated for less than 20 Ma (red and yellow areas in Fig. A5a$_2$).

For the SH+MH.5 model, the first episode of growth occurs at approximately 22 Ma and the second occurs at approximately 47 Ma (Figs A5b$_1$ and b$_3$). The first episode is associated with secondary areas that remain hydrated for periods between 20 and 30 Ma (blue areas in Fig. A5b$_1$), while the second episode is associated with secondary areas that remain hydrated for periods between 10 and 20 Ma (yellow areas in Fig. A5b$_3$). After the collision, a third episode between 52 and 56 Ma occurs and defines the dominant hydration zone during the post-collisional phase (Fig. A5b$_4$).

The extension of the hydrated area of the SH+MH.8 model shows only one maximum at approximately 27 Ma (P$_{8.1}$ in Fig. 8b). This is related to the more stable thermal field that characterizes the active oceanic subduction phase of the high velocity model. This episode is associated with secondary areas that remain hydrated for periods between 10 and 30 Ma (yellow and blue areas in Fig. A5c$_2$) and contributes to the expansion in depth and towards the external portion of the main hydrated area (Fig. A5c$_2$).

At the collision, the hydrated area decreases abruptly by approximately 500 km^2 in the SH+MH.3 and SH+MH.5 models and by approximately 750 km^2 in the SH+MH.8 model (red, green and blue lines in Fig. 8b, respectively). This decrease follows the partial subduction of the continental crust of the lower plate, which confines the low viscosity hydrated channel between the upper plate and the subducting lithosphere. Another important change in the boundaries of the hydrated area occurs after the collision in the SH+MH.8 model and it is associated with the secondary areas that remain hydrated for periods between 1 and 20 Ma (red and yellow areas in Figs A5c$_3$ and c$_4$); it results in an increase of approximately 1000 km^2 that persists for 10 Ma (Fig. A5c$_3$). This change contrasts with the decreased extension of the main hydrated area and controls the marginal widening of the hydrated area of approximately 775 km^2 (Fig. A5c$_4$).

During the early stages of the post-collisional phase, the hydrated area of all models gradually decreases. In addition, the hydration during the post-collisional phase lasts for longer times in the SH+MH.8 model (blue line in Fig. 8b) compared with that of the SH+MH.3 and SH+MH.5 models (red and green lines in Fig. 8b, respectively), resulting from the lower temperatures that characterize the wedge area in the high velocity model because of the higher subduction rates before continental collision.